

**AGH**

**AKADEMIA GÓRNICZO-HUTNICZA IM. STANISŁAWA STASZICA W KRAKOWIE**

**WYDZIAŁ INFORMATYKI, ELEKTRONIKI I TELEKOMUNIKACJI  
KATEDRA ELEKTRONIKI**

**PRACA DYPLOMOWA INŻYNIERSKA**

**DEVELOPMENT OF CALIBRATION STAND FOR MOSFET  
TRANSISTORS WORKING AS IONIZING RADIATION  
SENSORS.**

**BUDOWA STANOWISKA KALIBRACYJNEGO DLA TRANZYSTORÓW  
MOSFET PRACUJĄCYCH JAKO CZUJNIKI PROMIENIOWANIA  
JONIZUJĄCEGO.**

AUTOR: Michał Gumiela

KIERUNEK STUDIÓW: Electronics and Telecommunications

OPIEKUN PRACY: dr inż. Cezary Worek

Kraków 2017

## **OŚWIADCZENIE AUTORA PRACY**

UPRZEDZONY O ODPOWIEDZIALNOŚCI KARNEJ NA PODSTAWIE ART. 115 UST. 1 i 2 USTAWY Z DNIA 4 LUTEGO 1994 R. O PRAWIE AUTORSKIM I PRAWACH POKREWNYCH (T.J. Dz.U. z 2006 r. poz. 631 z późn. zm.): „KTO PRZY-WŁASZCZA SOBIE AUTORSTWO ALBO WPROWADZA W BŁĄD CO DO AUTORSTWA CAŁOŚCI LUB CZĘŚCI CUDZEGO UTWORU ALBO ARTYSTYCZNEGO WYKONANIA, PODLEGA GRZYNIE, KARZE OGRANICZENIA WOLNOŚCI ALBO POZBAWIENIA WOLNOŚCI DO LAT 3. TEJ SAMEJ KARZE PODLEGA, KTO ROZPOWSZECH-NIA BEZ PODANIA NAZWISKA LUB PSEUDONIMU TWÓRCY CUDZY UTWÓR W WERSJI ORYGINALNEJ ALBO W POSTACI OPRACOWANIA, ARTYSTYCZNE WYKONANIE ALBO PUBLICZNIE ZNIEKSZTAŁCA TAKI UTWÓR, ARTYSTYCZNE WYKONANIE, FONOGRAM, VIDEOGRAM LUB NADANIE.”, A TAKŻE UPRZEDZONY O ODPOWIEDZIALNOŚCI DYSCYPLINARNEJ NA PODSTAWIE ART. 211 UST. 1 USTAWY Z DNIA 27 LIPCA 2005 R. PRAWO O SZKOLNICTWIE WYŻSZYM (T.J. Dz. U. z 2012 r. poz. 572, z późn. zm.) „ZA NARUSZENIE PRZEPISÓW OBOWIĄZUJĄCYCH W UCZELNI ORAZ ZA CZYNY UCHYBIAJĄCE GODNOŚCI STUDENTA STUDENT PONOSI ODPOWIEDZIALNOŚĆ DYSCYPLINARNĄ PRZED KOMISJĄ DYSCYPLINARNĄ ALBO PRZED SĄDEM KOLEŻEŃSKIM SAMORZĄDU STUDENCKIEGO, ZWANYM DALEJ „SĄDEM KOLEŻEŃSKIM”, OŚWIADCZAM, ŻE NINIEJSZĄ PRACĘ DYPLOMOWĄ WYKONAŁEM(-AM) OSOBIŚCIE, SAMODZIELNIE I ŻE NIE KORZYSTAŁEM(-AM) ZE ŹRÓDEŁ INNYCH NIŻ WYMIESZCZONE W PRACY.

.....  
PODPIS

# Contents

<b>1. Terms, definitions and abbreviations .....</b>	<b>5</b>
1.1. Definitions .....	5
1.2. Abbreviations.....	5
<b>2. Introduction.....</b>	<b>7</b>
2.1. Background.....	7
2.2. Objectives .....	8
<b>3. Ionizing radiation principles.....</b>	<b>9</b>
3.1. Radiation environment in low-Earth orbit.....	9
3.2. Radiation influence on electronic devices .....	9
3.3. Total ionising dose modelling and monitoring in spacecraft missions.....	11
<b>4. Metal-Oxide Field Effect Transistor - based TID sensor .....</b>	<b>13</b>
4.1. Ionizing radiation influence on MOSFET transistors.....	13
4.2. Conceptual design of TID radiation sensor .....	14
4.3. Radiation-sensitive P-MOSFET transistors selection .....	14
4.3.1. Review of available radiation-sensitive P-MOSFETs.....	14
4.3.2. Threshold voltage extraction.....	15
4.3.3. Temperature compensation .....	17
<b>5. Test and calibration stand design .....</b>	<b>20</b>
5.1. Design assumptions .....	20
5.2. Block diagram of the stand.....	21
5.3. Electronic design .....	23
5.3.1. Threshold voltage extraction and die temperature measurement circuits.....	23
5.3.2. Reference temperature measurement.....	26
5.3.3. Microcontroller unit.....	30
5.3.4. Communication interfaces .....	31
5.3.5. Power supply.....	33
5.3.6. Printed circuit boards design.....	33
5.4. Software design .....	34

5.4.1. Embedded software for AVR MCU .....	34
5.4.2. Embedded software for ESP8266 MCU .....	35
5.4.3. PC control software for the stand.....	35
<b>6. Test and calibration stand performance .....</b>	<b>41</b>
6.1. Current source characteristics.....	41
6.2. P-MOSFET characterisation .....	41
6.2.1. I-V characteristic.....	41
6.2.2. Threshold voltage noise measurement.....	41
6.2.3. Temperature calibration .....	42
6.3. N-MOSFET body diode characterisation .....	42
6.3.1. Temperature calibration .....	42
<b>7. Calibration procedures.....</b>	<b>50</b>
7.1. Temperature dependence calibrations .....	50
7.2. Zero-temperature coefficient current determination.....	51
7.3. Ionising radiation influence calibration .....	51
<b>8. Summary.....</b>	<b>53</b>
Bibliography .....	57

# 1. Terms, definitions and abbreviations

## 1.1. Definitions

- **Total ionizing dose** – the portion of the energy absorbed by a matter during the whole time of exposure on ionizing radiation. [12] Expressed in grays (Gy) or rads (Rad). 1 Gy = 100 Rad.
- **Zero-temperature coefficient current** – a drain current of a MOSFET transistor at which its threshold voltage exhibits the lowest (ideally zero) temperature dependence.
- **CubeSat** – a pico- or nano- satellite, composed of multiples 10 x 10 x 11.35 cm cubic units, each of a 1.33 kg mass. Frequently build by university students, for educational and research purposes. For instance 2U CubeSat has a volume and mass of two units. [7]
- **RadFET** – common name for specialized, radiation sensitive P-MOSFET transistors used in TID measurements.
- **Low Earth orbit** – an orbit with an altitude between 180 km and 2000 km. Most scientific and observatory satellites are located at the low Earth orbit.[35]
- **Dosimeter** – a sensor that measures exposure to ionising radiation.

## 1.2. Abbreviations

- **A/D** – Analog/Digital
- **ADC** – Analog to Digital Converter
- **CCS** – Constant Current Source
- **CM** – Common Mode
- **COTS** – Commercial Off-The-Shelf
- **D/A** – Digital/Analog
- **DAC** – Digital to Analog Converter
- **DM** – Differential Mode

- **DUT** – Device Under Test
- **GPIO** – General Purpose Input Output
- **IC** – Integrated Circuit
- **I/O** – Input/Output
- **LCL** – Latch-up Current Limiter
- **LEO** – Low Earth Orbit
- **LDO** – Low-Dropout regulator
- **LSB** – Least Significant Bit
- **MCU** – Micro-Controller Unit
- **PCB** – Printed Circuit Board
- **PSU** – Power Supply Unit
- **RadFET** – Radiation Sensitive Field Effect Transistor
- **RTD** – Resistance Temperature Detector
- **SEE** – Single Event Effect
- **SEL** – Single Event Latch-up
- **SEU** – Single Event Upset
- **SoC** – System On a Chip
- **TID** – Total Ionizing Dose
- **UART** – Universal Asynchronous Receiver/Transmitter
- **VCCS** – Voltage-Controlled Current Source
- **ZTC** – Zero Temperature Coefficient

## 2. Introduction

### 2.1. Background

Ionising radiation monitoring is a serious concern in both manned and unmanned spacecraft missions, either on Earth orbit or extraterrestrial. Since cosmic radiation is a hazard for people and other biological organisms as well as electronic systems, several different radiation dosimetry methods have been designed so far, fulfilling needs for particular mission. Although dosimetry devices are common even in unmanned spacecrafts (e.g. satellites, probes), usually they lack in small, educational and research satellites, especially CubeSats. There are many reasons for such situation. At first, radiation monitoring devices are not essential part in terms of spacecraft survival, hence due to volume, mass and price limitations, such systems are not a common part of CubeSats. Another important issue is lack of ready-made CubeSat-compatible radiation sensors available on the market. Even though, the CubeSat are mostly deployed on low Earth orbit where radiation level is relatively small and mission duration is shorter comparing to commercial or governmental missions, they are composed of commercially available, non-radiation hardened components, thus far more susceptible to radiation-related damages. Although there have been developed models for radiation environment predictions, the results are not always in line with actual in-orbit observations. Geometry and shielding of a spacecraft and actual solar activity have also a serious impact.



Figure 2.1: A render of PW-Sat2 internals. [32]

During the phase of payload definition on board of PW-Sat2 2.1, 2U CubeSat [44], a possibility of development of small, low-cost, low-power, dose-integrating dosimetry system for the CubeSat on low Earth orbit has been investigated. The CubeSat is fully based on commercially available components, what is more, some of them without heritage (flight history), thus in-orbit radiation data will develop knowledge about their survival and operation. Feasibility studies have confirmed that commercially available metal-oxide field effect transistors are great candidates for total ionising dose sensors. However, the transistors not only have to be equipped with read-out circuitry, but also their characteristics have to be determined experimentally. Thus, in order to test, characterize and carry out measurements on the selected radiation-sensitive transistors an idea of a test and calibration stand has came to thesis author's mind.

## 2.2. Objectives

The main objective of the thesis, as explained in the previous chapter, was to design and build test and calibration stand for radiation sensitive P-MOSFET transistors. Additionally, the stand should be used for N-MOSFET body diode calibration for temperature measurements.

The stand comprises biasing and read out modules for measurements of threshold voltage of the transistors, forward diode voltage and reference thermometers for thermal calibrations, controlled by a microcontroller. Resolution and accuracy of the circuits have to meet expectations defined by the conceptual radiation sensor for the PW-Sat2 satellite. The project includes also development of a PC application for data acquisition.

As the result of the thesis fully-functional and ready to use test and calibration stand for transistors characterisation is presented.

## 3. Ionizing radiation principles

The chapter deals with a description of a specific radiation environment in low Earth orbit. The effects of such specific and harsh conditions on spacecraft electronic devices is briefly discussed. Then selected tools for predicting absorbed dose amount during the spacecraft mission and types of popularly used sensors are introduced.

### 3.1. Radiation environment in low-Earth orbit

Natural radiation environment in low-Earth orbit is a complex mixture of transient galactic cosmic rays (mainly protons and heavy ions), Solar particle events (protons and heavy ions), trapped particles (protons, electrons and heavy ions) in the belts and induced in an atmosphere secondary particles (mainly neutrons) [10] [36].

The **galactic cosmic rays** originate outside the solar system. Although relatively low fluxes of the cosmic rays, heavy ions cause intense deposition of energy as they pass through matter. Because of their high energy, shielding is not sufficient to eliminate the risk, resulting mainly in single event effects. [1]

**Solar particles** flux, including electrons, protons and heavier charged particles (up to iron), is emitted during solar flares and corona mass ejections. However these events are relatively rare, occurring during the solar maximum phase of the 11-year solar cycle, thus some space crafts might even not experience such an event. [18]

**Trapped particle belts**, known as The Van Allen radiation belts, consist mainly of electrons (energy of a few MeV) and protons (energy up to hundreds of MeV), which are trapped in the Earth's magnetic field. Additionally the Bremsstrahlung (X-Ray) radiation is produced as a result of decelerating charged particles. There are two belts which are located in the inner region of the Earth's magnetosphere. [1] The inner belt extends typically from an altitude of about 650 km to 10,000 km [34], partially overlapping with the LEO (180 - 2000 km) [35]. However, even for orbits below typical range for the inner belt, trapped radiation is a significant concern because of The South Atlantic Anomaly (SAA), where the belt dips down to an altitude of 200 km - see Fig. 3.1.

### 3.2. Radiation influence on electronic devices

Commonly ionising radiation is considered as an important factor for biological organisms. Although relatively low doses, like natural background radiation, can be even beneficial [16], high absorbed doses are fatal. But not only living matter has to be protected against radiation. Surprisingly, the electronic semiconductor devices can suffer from radiation-related problems as well. Ionising radiation effects in solid-state electronic devices can be

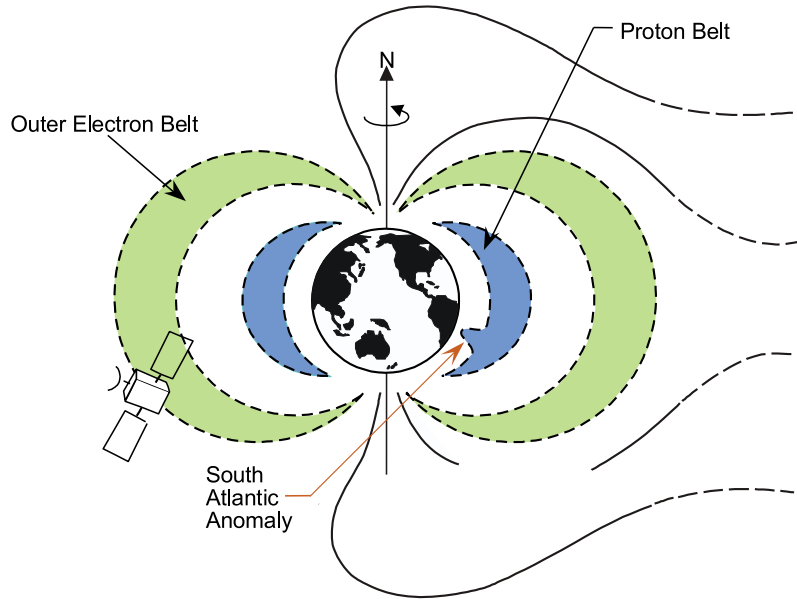


Figure 3.1: The Earth's Van Allen trapped particle belts with the South Atlantic Anomaly. [30]

divided into two general categories: cumulative effects gradually changing parameters of the devices and single event effects causing abrupt changes.[39]

The ionising radiation may have a form of particles or photons that have enough energy to penetrate and deposit energy in a solid state matter. This can change the electrical parameters and characteristics of irradiated device and then, after longer period of dose accumulation can lead to malfunctions. This effect is commonly referred as Total Ionising Dose (TID) damage. The TID affects a couple of parameters of CMOS devices, among others: threshold voltage, an increase of leakage current, deterioration of noise parameters, a reduction of drain-source breakdown voltage. [12] Another long-term effect degrading electronic devices, called displacement damage is caused by high-energy protons, electrons and neutrons. However, it is a non-ionising damage, caused by the collisions between incoming particles and lattice displacing an atom from its position.

Besides, **Single Event Effects (SEE)** might occur as well. The SEE is caused by strike of a single, high-energetic particle. The SEEs can be divided into two categories: destructive SEE and non-destructive SEE. The first of SEE type is a non-destructive, so-called **Single Event Upset (SEU)**, which basically is a change of a storage cell state (soft error) caused by a single event. The SEU is not considered as damaging effect for silicon structure, but it might change a behaviour of the entire system. The other single event effect is a **Single Event Latch-up (SEL)**. In case of the SEL, energy deposited by a particle affects parasitic CMOS structures ( $pnnp$ ), i.e. turns on thyristor structure causing a short circuit between supply and ground rails. A power-cycle is needed to bring the structure to normal state. However, SEL can be fatal for the device. [45] [12]

There are many methods for mitigation of SEE, including system-level and equipment level solutions. Non-destructive SEU in memory or data streams can be handled by a proper design of the whole system (data redundancy, correction coding, voting mechanisms in microprocessor circuits). Potentially destructive SELs can be limited by utilization of supervisory circuits called latch-up current limiters (LCL), switching off a device when a sharp increase of current flow is detected. [8] In turn, a TID can be limited by the addition of shielding but its influence cannot be completely mitigated. Systems working in harsh, high-radiation level environment have to

comprise of designed or tested for radiation immunity (rad hard) components.[39]

### 3.3. Total ionising dose modelling and monitoring in spacecraft missions

The first spacecraft failure caused by a total ionising dose was telecommunication satellite Telestar 1, launched on July 10, 1962. [46] During near of half century of space exploration there were numbers of failures and system malfunctions caused by radiation. [40] In order to predict dose levels absorbed by a spacecraft various models were developed. One of the available pieces of computer software is ESA's SPENVIS (The Space Environment Information System). Among others, it has functionalities of spacecraft trajectory generator and utilizes SHIELDOSE models for computation of absorbed dose behind aluminium shielding of a spacecraft. Exemplary results for the PW-Sat2 CubeSat are presented in Figure 3.2.

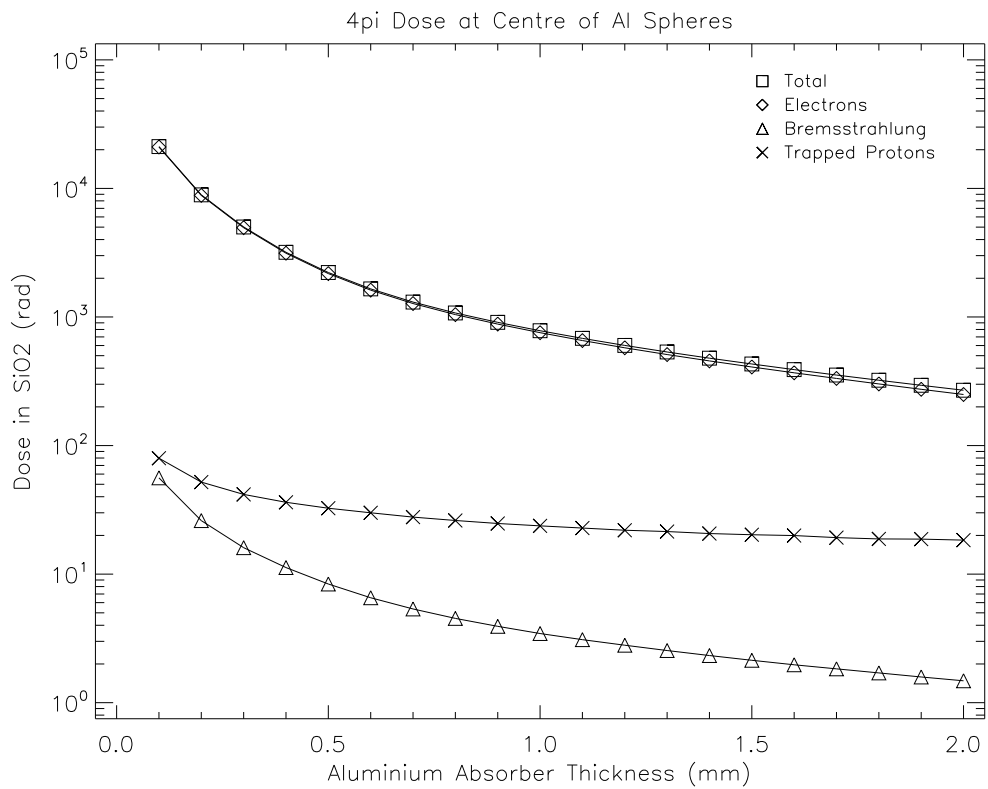


Figure 3.2: SPENVIS simulation of TID vs. shielding depth. Components from various types of radiation are distinguished. [20]

Although total ionisation doses can be estimated thanks to software simulations, research and measurements of actually absorbed doses are still carried out. Various types of detectors can be used, dependently on specific conditions of measurement and demands. As the first example of TID detector, a thermoluminescent dosimeter (TLD) can be recalled. Off-line measurements utilizing such dosimeters are commonly carried out aboard the International Space Station (ISS). TLD pills after desired period of irradiation are read out in space or transferred to the Earth. [47] Another popular methods utilizes various CMOS circuits and investigate variations in electric parameters of the circuits as a function of TID. The most common solution is based solely on P-MOSFET transistors. These sensors achieve sufficient sensitivity for a spectrum of applications, allow for on-line, remote measurement.

Moreover a P-MOSFET-based sensor can be completely passive, i.e. turned off during irradiation process. The rest of the thesis is focused on P-MOSFET based TID sensor.

## 4. Metal-Oxide Field Effect Transistor - based TID sensor

The chapter deals with a theoretical introduction to the TID radiation sensors based on P-channel Metal-Oxide Field Effect Transistors, popularly known as RadFETs. Ionising radiation effects on the characteristics of a MOSFET transistors are briefly discussed (considering a threshold voltage as a main parameter). Later, a topology and assumptions of conceptual TID sensor proposed in the thesis developed at The Department of Electronics AGH-UST [20] is presented and finally, measurement techniques of required quantities and parameters are discussed.

### 4.1. Ionizing radiation influence on MOSFET transistors

In principle, utilization of MOSFET transistors in dosimetry is based on examination of the threshold voltage shift,  $\Delta V_{Th}$ , induced by the radiation,  $D$ . This dependence can be described by the Equation 4.1. [43]

$$\Delta V_{Th} = A \cdot D^n \quad (4.1)$$

where:

$\Delta V_{Th}$  - threshold voltage shift

$A$  - proportionality factor

$n$  - linearity coefficient

$D$  - absorbed dose

Quanta of ionizing radiation possess enough energy to induce the electron-hole pairs in transistor oxide regions. Since effective mobility of electrons in  $\text{SiO}_2$  is significantly higher than holes, they can easily sweep out of the gate oxide region, avoiding recombination. In turn, holes transportation through the oxide is much slower and some of them can be trapped in long-term sites in the oxide region (if the oxide is thick enough), producing positive charge build-up.[5] Moreover, other holes might move to the silicon-oxide region where they create the interface traps.[4] Both effects contribute to  $V_{Th}$  shift. In P-MOSFET devices  $V_{Th}$  change caused by these effects occurs in the same direction, whereas in N-MOSFET devices both effects compensate each other, hence practically P-MOSFETs are used in dosimetry. [43] The phenomenon can be described by the Equation 4.2.[5] The sensitivity is mostly dependent on gate oxide thickness, thus the transistors with thin gate oxide region are not suitable for dosimetry purposes.

$$\Delta V_{Th} = -\frac{\Delta Q_{ot} + \Delta Q_{it}}{C_{ox}} \quad (4.2)$$

where:

- $\Delta V_{Th}$  - threshold voltage shift
- $\Delta Q_{ot}$  - charge trapped in the oxide region (positive)
- $\Delta Q_{it}$  - charge trapped in the interface states, positive for P-MOSFETs and negative for N-MOSFETs
- $C_{ox}$  - the oxide capacitance

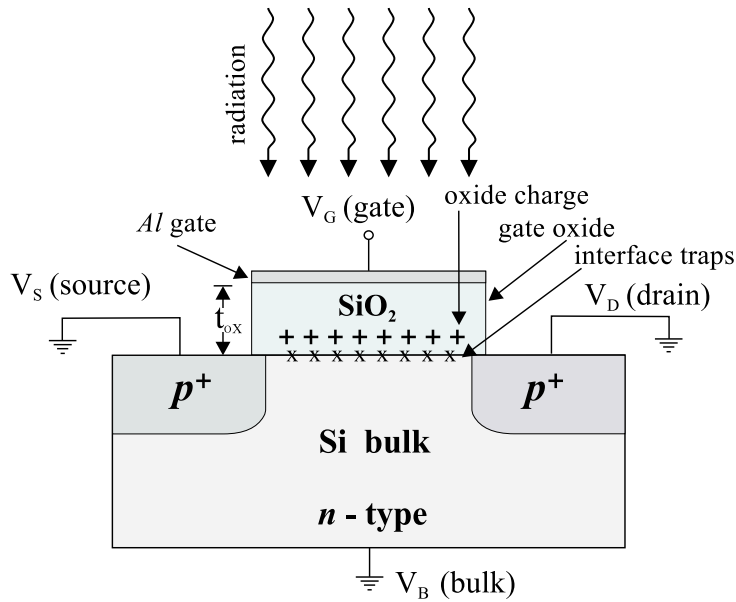


Figure 4.1: MOSFET transistor during irradiation. [43]

## 4.2. Conceptual design of TID radiation sensor

Calibration stand described in the thesis is intended to deliver all needed characteristics of transistors that are used in a TID sensor proposed in [20]. In order to do so, the calibration stand has to be strictly designed for P-MOSFET transistors used by the sensor. Performance of the stand (i.e. calibration accuracy) has to meet the requirements specified for the sensor.

Expected parameters of the sensor [20] are summed up in Table 4.1. A design of the calibration stand has to take them into account to allow for calibration within assumed range, with desired resolution and accuracy.

## 4.3. Radiation-sensitive P-MOSFET transistors selection

### 4.3.1. Review of available radiation-sensitive P-MOSFETs

Generally, P-MOSFET transistors aimed as TID sensors are called RadFETs. [12] RadFETs are designed and produced in several laboratories and institutes, in various configurations, sensitivity and measurement ranges. [20] However, there are numbers of journal articles proving that commercially available (so-called COTS) P-MOSFET

Table 4.1: Expected parameters of proposed sensor [20]

Range	100 Gy (10 kRad)
Resolution	0.1 Gy
Accuracy	$\pm 1.0 \text{ Gy}$
Calibrated temperature range	+20 ... +50 °C
Operating temperature range	-40 ... +125 °C

transistors might be used for TID dosimetry. For the sensor purposes different models of COTS transistors with reported radiation sensitivity have been compared in [20], namely: Siliconix 3N163 [28], Zetex Semiconductors ZVP3306 [28], ZVP4525, BS250F [41] [33] and Texas Instruments CD4007 [11] [6]. As a trade-off between sensitivity, device physical dimensions, initial value of threshold voltage and a price, Texas Instruments CD4007 integrated circuit consisting of several transistors was chosen. [20].

#### Texas Instruments CD4007 integrated circuit specification

A CD4007 transistor array comprises of six MOSFET transistors - three P-channel and three N-channel. Internal connections between transistors and externally available terminals are shown in Figure 4.2. With a proper connection, all three P-MOSFET transistors are viable to be used in a dosimeter circuit. Available publications indicate sensitivity of about  $5 \text{ mV/Gy}$  in unbiased mode (Fig. 4.3) and possibility of temperature compensation utilizing several different techniques, including zero-temperature coefficient current readout biasing ( $I_{ZTC}$ ).[5]

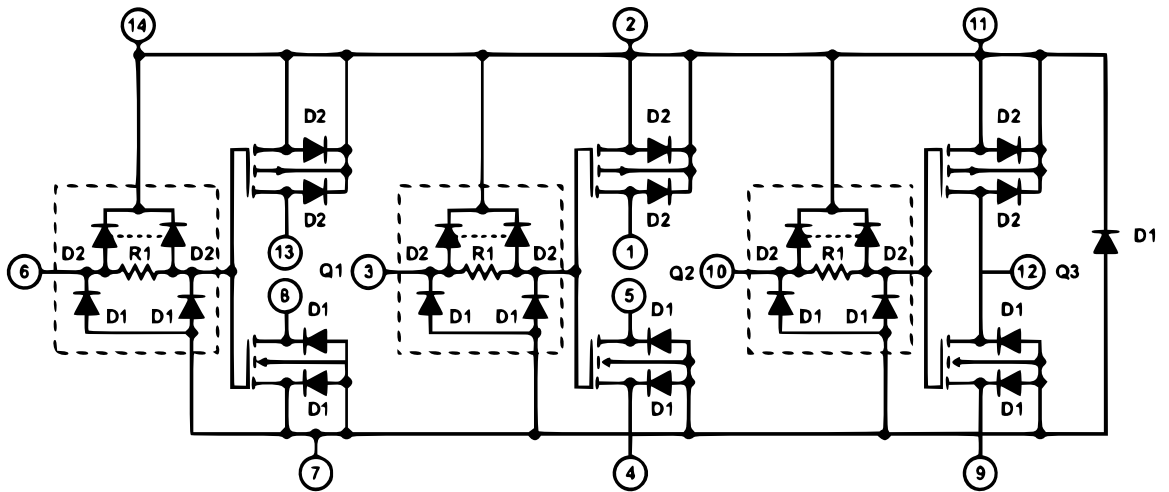


Figure 4.2: A schematic of a CD4007 integrated transistor array. [13]

#### 4.3.2. Threshold voltage extraction

Generally, the threshold voltage is seen as a gate voltage at which significant drain current starts to flow, but not single and exact definition of  $V_{Th}$  can be given. [42] Since for dosimetric purposes only shifts in  $V_{Th}$  have significant meaning, all consideration in the dissertation are carried out in a such direction. A widely used in

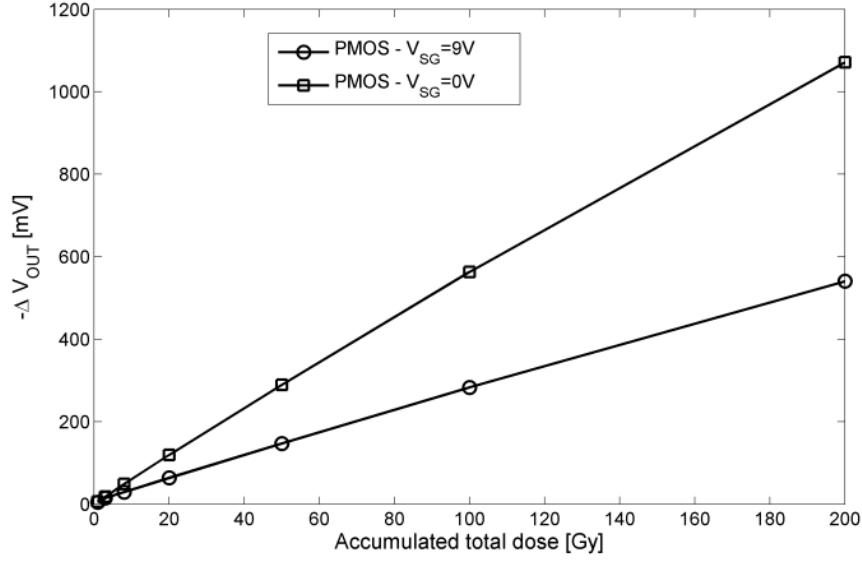


Figure 4.3: Radiation response of CD4007's P-MOSFET in biased and unbiased modes. [6]

Table 4.2: Parameters of CD4007 integrated circuit.

Device type	integrated transistor array; 3 x P-MOSFET, 3 x N-MOSFET
Initial $V_{Th}(I_D)$	$\tilde{2.0} \text{ V}$ @ $100 \mu\text{A}$
Operating-temperature range	$-55 - 125^\circ\text{C}$
Package	TSSOP-14
Physical dimensions (W x L x H)	$4.4 \times 5.0 \times 1.2 \text{ mm}$

industry technique is the constant current method. In principle, the method evaluates  $V_{Th}$  as the value of  $V_{gs}$  at some chosen, constant drain current  $I_D$ . [42]

The constant current method gained popularity because of its simplicity in comparison to other methods such as extraction from  $I_D - V_{gs}$  curve.[42] Nonetheless, it has some drawbacks. The most important is a fact that changes in a drain current have a reflection in changes of  $V_{gs}$ . Instability of the biasing current source might introduce an error into measurements, hence a special care must be taken to this issue. In order to increase a stability of the system, P-MOSFET should operate in a saturation mode where relationship between drain current and gate voltage is unaffected by a gate-drain bias voltage. To put a transistor in a saturation regime a gate-source voltage ( $V_{gs}$ ) has to be greater than a threshold voltage ( $V_{Th}$ ), concurrently, a drain-source voltage ( $V_{ds}$ ) has to be also greater than a  $V_{Th}$ . Those two conditions are summed up in Equation 4.3. It has to be noted, that although the  $V_{Th}$  parameter in P-MOSFET devices is negative, in the further chapters of the thesis always an absolute value is considered. The same holds for drain current  $I_D$ .

$$V_{ds} > V_{gs} - |V_{Th}| \quad (4.3)$$

For a transistor in a saturation regime an  $I_D(V_{GS})$  relationship given by an Equation 4.4 holds. [29] After

solving for  $V_{Th}$  the equation has such a form 4.5. Since  $I_D = \text{const.}$  and changes in carrier mobility (hidden in  $\beta$  parameter) can be neglected [2], it might be proven that shift in  $V_{Th}$  has a reflection in  $V_{gs}$  in a predictable manner - Equation 4.6.

$$I_D = \frac{\beta}{2} (V_{gs} - V_{Th})^2 \quad (4.4)$$

$$V_{Th} = V_{gs} - \sqrt{\frac{2 \cdot I_D}{\beta}} \quad (4.5)$$

$$\Delta V_{Th} = \Delta V_{gs} \quad (4.6)$$

A circuit presented in Figure 4.4 that ensures operation in a saturation mode was selected and adopted for measurements in the calibration stand.

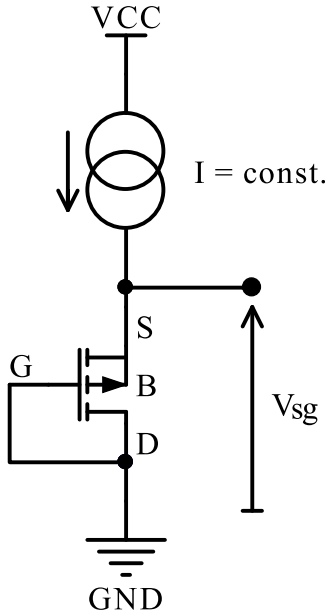


Figure 4.4: A P-MOSFET transistor operating in a saturation regime connected to a constant current source.

### 4.3.3. Temperature compensation

Due to significant influence of temperature on threshold voltage [37] it is necessary to compensate for this affection. The common approach is to determine  $V_{Th}$  variations due to temperature and then, providing a temperature measurement get rid of this dependence at the stage of data processing. The crucial point is a technique used for temperature measurement. One of the possible solutions is to attach additional, external temperature sensor placed close to the CD4007 integrated circuit. Such approach is an easy and reliable, but does not provide exact measurement of the temperature of P-MOSFETs in the CD4007. In a design of the TID sensor described in [20], a different solution to this problem has been proposed. Since P-MOSFETs and N-MOSFETs in CD4007 are placed on the same silicon die and no significant heat is dissipated in the circuit, an assumption that the whole die remains in a thermal equilibrium holds. Those facts make a  $p - n$  junction of a N-MOSFET transistor (namely, a

body diode) an ideal candidate for temperature-sensing device. The variations of the body diode's forward voltage caused by a temperature changes have to be calibrated. The proposed circuit is presented in Figure 4.5.

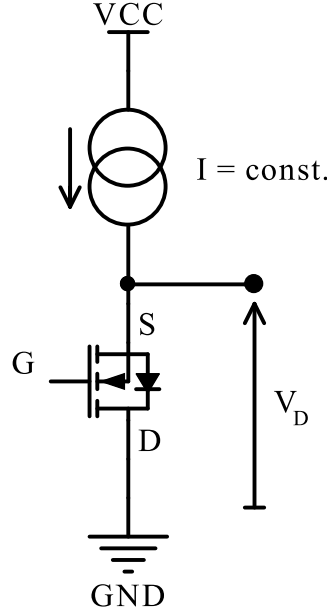


Figure 4.5: A circuit utilizing a body diode of N-MOSFET transistor for temperature measurement.

### Diode's forward voltage temperature dependence

A drain current in a silicon diode might be described by the Shockley ideal diode equation (Eq. 4.7). A reverse bias saturation current ( $I_S$ ) in the equation is also temperature-dependent (Eq. 4.8). Although, solving the equation for diode's forward voltage  $V_D$ , leads to a complex dependence (Eq. 4.9), several approximations are available in a limited temperature range. As a first approximation, an exponential component in Eq. 4.9 might be neglected because of its small value in a temperature range of interests,[22] which leads to Eq. 4.10. Solving for  $T$ , gives Eq. 4.11. Provided  $I_D$  current is constant, variations of  $E_g$  due to temperature in considered range, the characteristic can be described by a linear dependence - Eq. 4.12. The linearisation of the characteristic significantly simplifies a calibration procedure.

$$I_D = I_S \left[ \exp \left( \frac{qV_D}{nk_B T} - 1 \right) \right] \quad (4.7)$$

where:

- $I_D$  - diode forward current
- $q$  - the electron charge
- $k_B$  - the Boltzmann's constant
- $T$  - a temperature of a p-n junction
- $V_D$  - diode's forward voltage
- $n$  - a quality factor

$$I_S = A \exp \left( -\frac{E_g}{2k_B T} \right) \quad (4.8)$$

where:

$I_S$  - diode reverse bias saturation current

$E_g$  - a semiconductor band gap

$A$  - a coefficient depending on a geometry and doping

$$V_D = \frac{\ln \left[ \frac{I_D}{A} + \exp \left( -\frac{E_g}{2k_B T} \right) \right] n k_B T + E_g}{q} \quad (4.9)$$

$$V_D \approx \frac{\ln \left( \frac{I_D}{A} \right) n k_B T + E_g}{q} \quad (4.10)$$

$$T \approx \left( V_D - \frac{E_g}{q} \right) \frac{q}{\ln \left( \frac{I_D}{A} \right) n k_B} \quad (4.11)$$

$$T(V_D) \approx V_D(T_0) + \alpha_T(T_a - T_0) \quad (4.12)$$

where:

$T_0$  - arbitrary reference temperature

$\alpha_T$  - temperature coefficient determined empirically

$T_a$  - actual temperature

## 5. Test and calibration stand design

The chapter addresses requirements and realization of the calibration stand for P-MOSFET transistors in all fields: electronics, software and mechanical design. In the following description all stages of the design are presented, beginning with the idea of subsystem, needs to be fulfilled, component selection, simulations, final electrical schematics and printed circuit boards. The final design is presented in Figure 5.1.

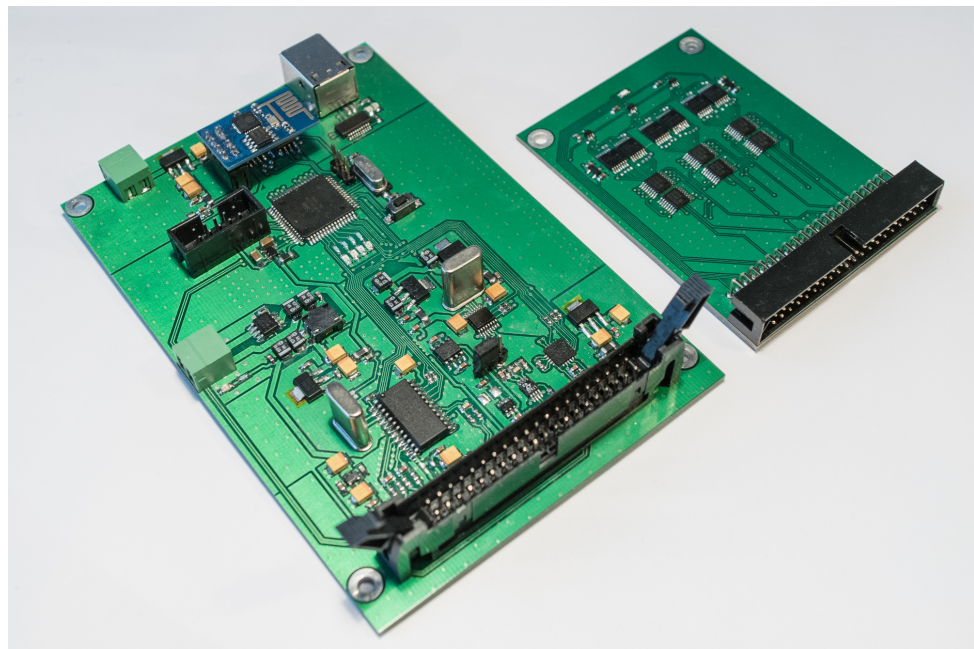


Figure 5.1: A picture of the test and calibration stand.

### 5.1. Design assumptions

In order to set down requirements to be met by the device, some general assumption were established. First of all, the calibration stand should allow to conduct precise measurements of P-MOSFET transistors' parameters needed to build TID sensor of the topology and performance presented in the chapter 4, namely:

- extraction of P-MOSFET transistors' threshold voltage (for examination of its long-term stability and on-line measurement during irradiation),
- temperature dependence of the threshold voltage (for further compensation of the influence),

- determination of zero-temperature coefficient biasing current ( $I_{ZTC}$ ) of the transistors (to use it as a one of temperature-compensation method),
- diode calibration for temperature measurements (for the purposes of  $V_{Th}$  temperature compensation).

Additionally, the stand has to be equipped with the interfaces allowing easy communication and data handling with a standard PC computer by a wired and range-expandable wireless connections. While the most of the calibration procedures can be carried out in a typical laboratory and a wired connection can be well used, the calibration for irradiation effects takes place in closed and shielded against ionizing radiation rooms, thus a wireless data connection is the best method to avoid a problematic, long-distant cabling between the calibration and control rooms.

In order to speed-up calibration procedure the stand should calibrate more than one transistor at the time. Moreover, the stand is expected to operate in harsh environment with significantly higher background radiation level, hence a special care must be taken during component selection.

## 5.2. Block diagram of the stand

The calibration stand is divided into two parts: main board and attachable cards. The main board contains the base subsystems. In turn, the card board contains P-MOSFET transistors for dosimetry along with a diode for temperature calibration (in the design within a single CD4007 integrated circuit), analog multiplexers and reference temperature sensors. A block diagram of the system is presented in Figure 5.2.

The idea behind the division of system into two parts in such manner has originated in several reasons. First of all, the stand should allow to calibrate dozens of transistors, hence the change of devices under calibration has to be affordable. Secondly, the readout part of the system (the main board) should be protected against a beam of ionising radiation used to calibrate the transistors. Shielding involving e.g. lead blocks is a widely used solution, so the transistors under examination and readout circuit have to be placed at least tens of centimetres apart. In order to minimize cabling between boards, analog multiplexers are placed right on the card board.

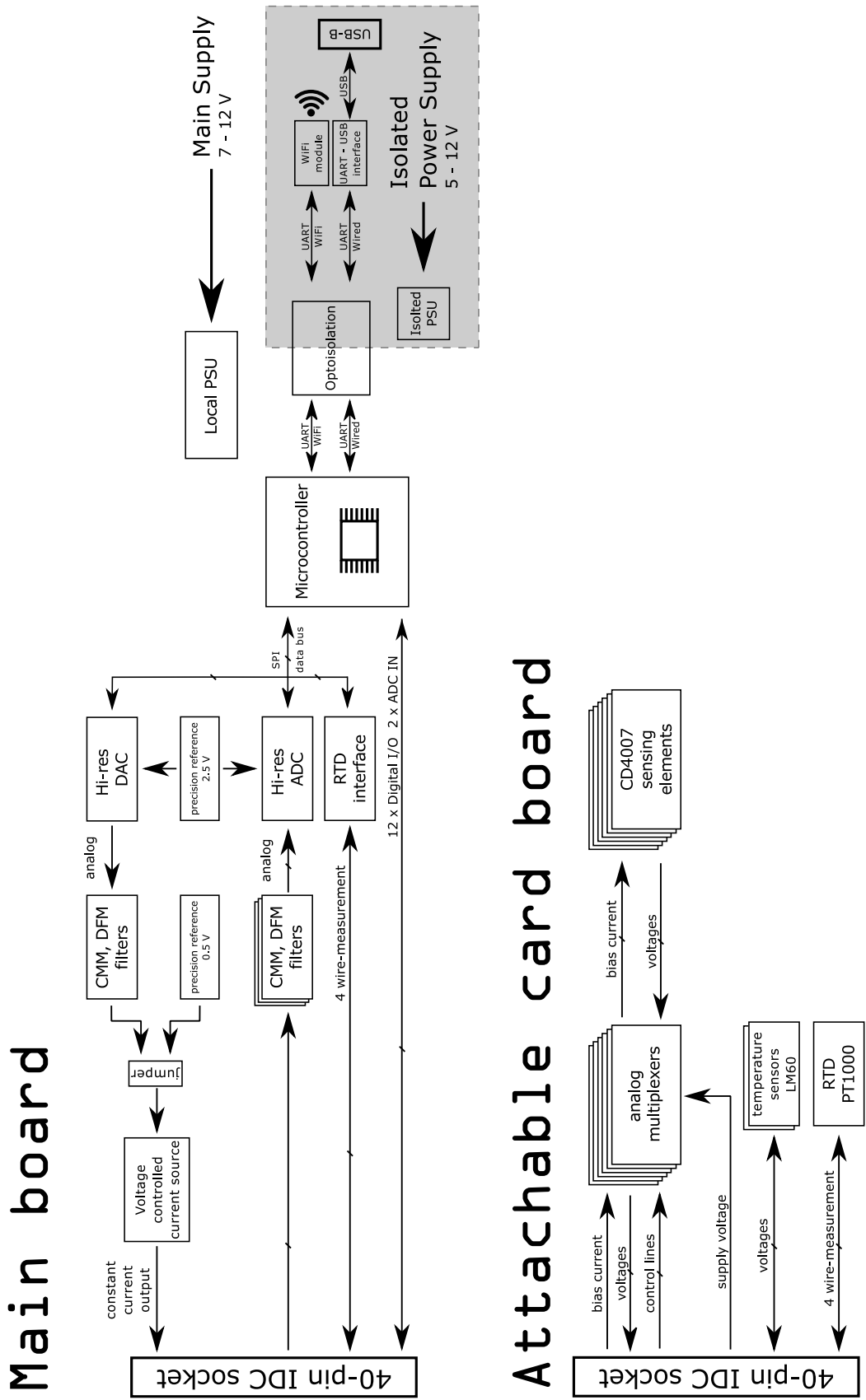


Figure 5.2: Block diagram of the calibration stand with the attachable card.

**The main board of the stand consists of following subsystems:**

- microcontroller unit,
- reference RTD thermometer interface,
- high-resolution analog-to-digital converter,
- digitally adjustable constant current source,
- optoisolated UART-USB communication interface,
- wireless network (WiFi) communication module,
- power distribution and filtering unit.

**The attachable card comprises of:**

- P-MOSFET transistors and diodes for temperature measurement (built-in CD4007 integrated circuits),
- analog multiplexers,
- reference thermometers: platinum RTD and LM60.

## 5.3. Electronic design

In this chapter issues related to electronic design of the calibration stand are discussed.

### 5.3.1. Threshold voltage extraction and die temperature measurement circuits

As described in detail in chapter 4, idea of total absorbed ionising radiation dose measurement (TID) by a P-MOSFET transistor is based on measurements of its threshold voltage shift caused by the radiation. It is crucial to measure this parameter in a precise, moreover automated and fast way. Additionally, the threshold voltage changes have to be compensated for temperature influence. While the method of extraction and die temperature measurement was discussed in chapters 4.3.2 and 4.3.3, at this point a practical implementation is provided.

#### Block diagram

Taking into account specific interconnections between transistors in the CD4007 integrated circuit and protective clamping diodes, a schematic connection presented in Figure 5.3 was proposed. It demands only one current source to bias all the transistors, one differential channel in A/D converter and analog multiplexers/switches. This layout can be expanded for more CD4007 by means of adding additional analog switches and/or A/D channels. In the stand design, as a trade off between complexity of the circuit and number of the CD4007 chips being calibrated at the time, the number of six CD4007 integrated circuits was chosen.

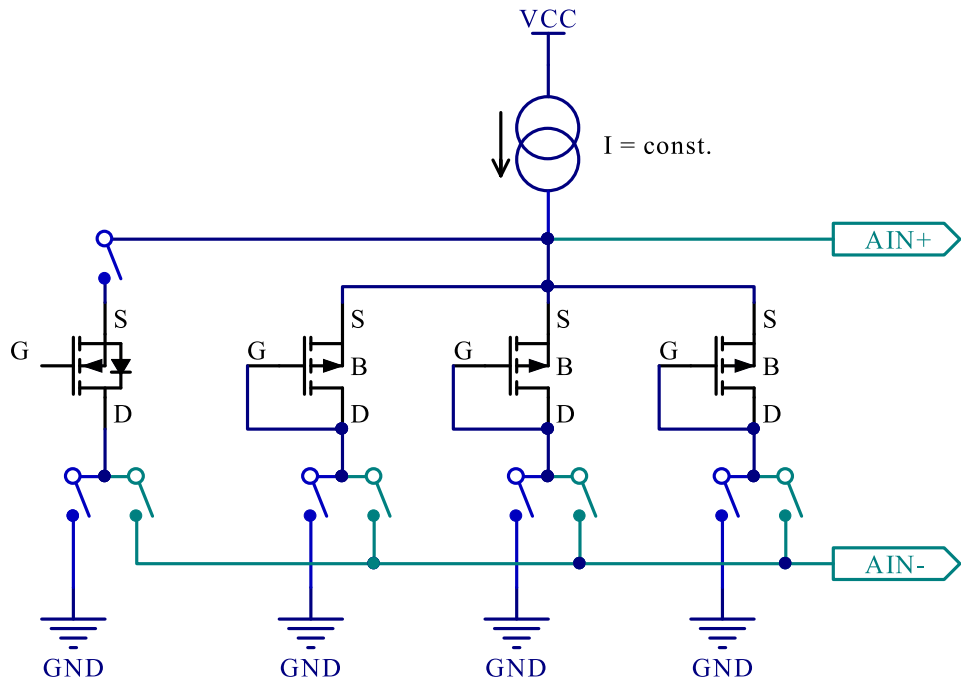


Figure 5.3: Connections of the transistors from the CD4007 integrated circuits.

### Precise voltage measurement

In order to measure analog signal, the AD7714YRZ from Analog Devices, 24-bit sigma-delta signal conditioning ADC was chosen. It has three fully differential inputs, 2.5 V differential input range, built-in high impedance buffer and tunnable, digital filter with a  $\text{Sinc}^3$  response. For desired resolution and range of voltage measurement  $0.25 \text{ mV/LSB}$  and  $2.5 \text{ V}$ , respectively, a 16-bit A/D converter would be sufficient, but this model was chosen because of differential inputs, built-in buffer assuring high input impedance, built-in digital filter, separated digital and analog power rails. Moreover, the part has been tested for ionizing radiation immunity, with the positive TID result up to  $7.5 \text{ kGy}$  without affection on its parameters. [19]

If not properly chosen, a reference voltage for the A/D converter would introduce significant gain error into measurements. Not only are initial accuracy, allowed output current, noise performance and long term stability important, but also a temperature coefficient have to be taken into account. To fulfil these requirements an ADR4520 from Analog Devices ultra-low noise, high initial accuracy ( $\pm 0.02\%$ ) and low temperature coefficient ( $2 \text{ ppm}/^\circ\text{C}$ ) voltage reference was selected.

Although the converter is equipped with a digital filter, that is applied after conversion, the external analog filters at the inputs were added. Taking into account long connections between ADC input and signal source, external filters, cutting out the noise prior to sampling are especially useful. A common mode/differential mode low-pass RC filters of the topology presented in Figure 5.4 were utilized. The results of AC response simulated in the LTSpice software is shown in Figure 5.5. Since the sampling frequency of the ADC is  $38 \text{ kHz}$ , the filter was designed to have significant attenuation at  $19 \text{ kHz}$  and up, namely  $-31 \text{ dB}$ .

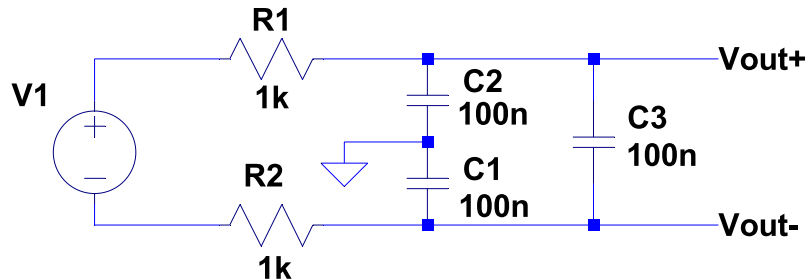


Figure 5.4: Schematic of the simulation of CM & DM filter.  $V_1$  is the signal source, while  $V_{out+}$  and  $V_{out-}$  are non-inverting and inverting inputs of the ADC, respectively.

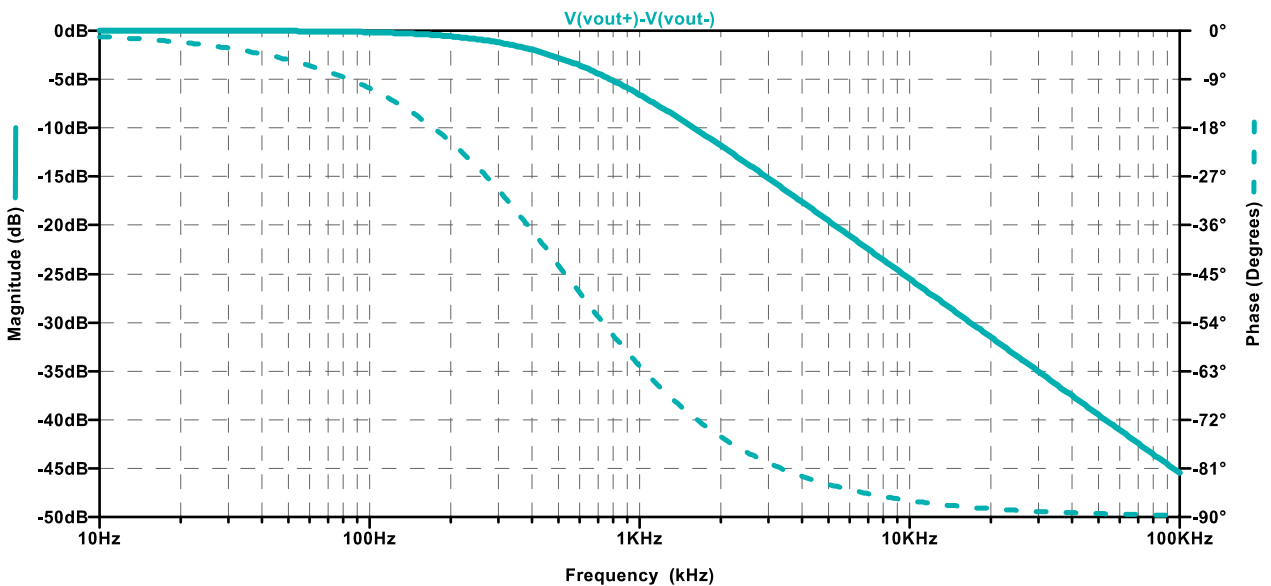


Figure 5.5: Results of the simulation of CM & DM filter.

### Voltage-controlled constant current source

For measurements of  $V_{Th}$  and its radiation and temperature dependences, body diode temperature calibration, a stable, low-noise constant current source providing a small, microampere-range current is a key component. Variations in constant current, caused e.g. by a temperature shift lead to changes in the operating point of biased devices by the source. Moreover, determination of  $I_{ZTC}$  and transfer characteristics demand adjustable constant current source. As the solution for those two needs - stable, not adjustable and digitally adjustable current source - the circuit presented in Figure 5.6 was adopted.[15] The circuit acts as a voltage controlled current source (VCCS), the output current is set by the  $V_{ctrl}$  voltage and  $R_{22}$  reference resistor, according to relationship  $I_{CCout} = V_{ctrl}/R_{Ref}$ . Since, the control voltage is present across the reference resistor, the maximum voltage at  $CCout$  node is positive op-amp rail  $V_{rail+} - V_{ctrl}$ . The  $V_{ctrl}$  can be provided either by a precision reference voltage source (for low-noise and stability) or D/A converter (for digitally controlled current source).

Simulations show that  $1 \mu A$  inaccuracy in the biasing current for P-MOSFET at operating point  $100 \mu$  would shift  $V_{gs}$  by  $2.4 mV$ , which is unacceptable. After calibration of the current source, a current should be known

with an accuracy of  $0.2 \mu\text{A}$ , at room temperature i.e.  $15 - 25^\circ\text{C}$ . There are several factors that have a reflection in the final accuracy and stability of the VCCS:

- **op-amps:** initial offset voltage and its variations with temperature, offset voltage shifts caused by TID;
- **reference resistor:** initial resistance accuracy, temperature coefficient;
- **controlling voltage:** initial accuracy, temperature coefficient.

Dual low-noise, rail-to-rail input/output LTC6078 operational amplifier from Linear Technology was chosen. An initial value of the current source and its gain error can be evaluated by means of calibration with external precision current meter, however thermal stability is crucial. In order to meet assumptions, as a reference resistor, a model with  $5 \text{ ppm}/^\circ\text{C}$  temperature coefficient was selected. As controlling voltage source, ADR130 from Analog Devices was chosen. Thermal simulations were performed in the LTSpice, the results are shown in Figure 5.7. The change in output current caused by the temperature variations are below  $0.1 \mu\text{A}$ .

As a control voltage for digitally adjustable mode of the current source, a precision, 20-bit sigma-delta D/A converter DAC1220 from Texas Instruments was selected. The DAC shares 2.5 V reference with the ADC AD7714, however the output range is from 0 - 5 V. The device has separate digital and analog supply rails. Communication is realized via SPI-like interface with the main AVR MCU. Theoretically the resolution of current setting is  $1 \tilde{n}\text{A}$ , however noise had been expected to dominate, so the effective accuracy of the VCCS was determined by means of calibration measurement with an external current meter.

### Analog switches / multiplexers

Analog multiplexer are placed on the card board, close to the CD4007 ICs. Therefore, they are affected by the temperature changes in wide range and high doses ionizing radiation. Considering non-zero and variable on resistance of selected analog multiplexers (ADG708 from Analog Devices), current and voltage paths were slitted (see Fig. 5.3). Exception from this method was made for N-MOSFET transistor, since the chosen analog switch has ultra low on resistance ( $0.5 \Omega$ ) and connected with it voltage offset is acceptable for temperature measurement (variations smaller than  $0.03^\circ\text{C}$ ).

### 5.3.2. Reference temperature measurement

A circuit of reference temperature measurement plays a main role for thermal characteristics determination. Desired range and accuracy of temperature measurement by a body diode in CD4007 integrated circuit point out requirements for reference temperature measurement circuit. The requirements are sum up in the table 5.1.

Table 5.1: Requirements for reference thermometer.

Resolution	$0.1^\circ\text{C}$
Accuracy	better than $1^\circ\text{C}$
Range	$0 - 150^\circ\text{C}$

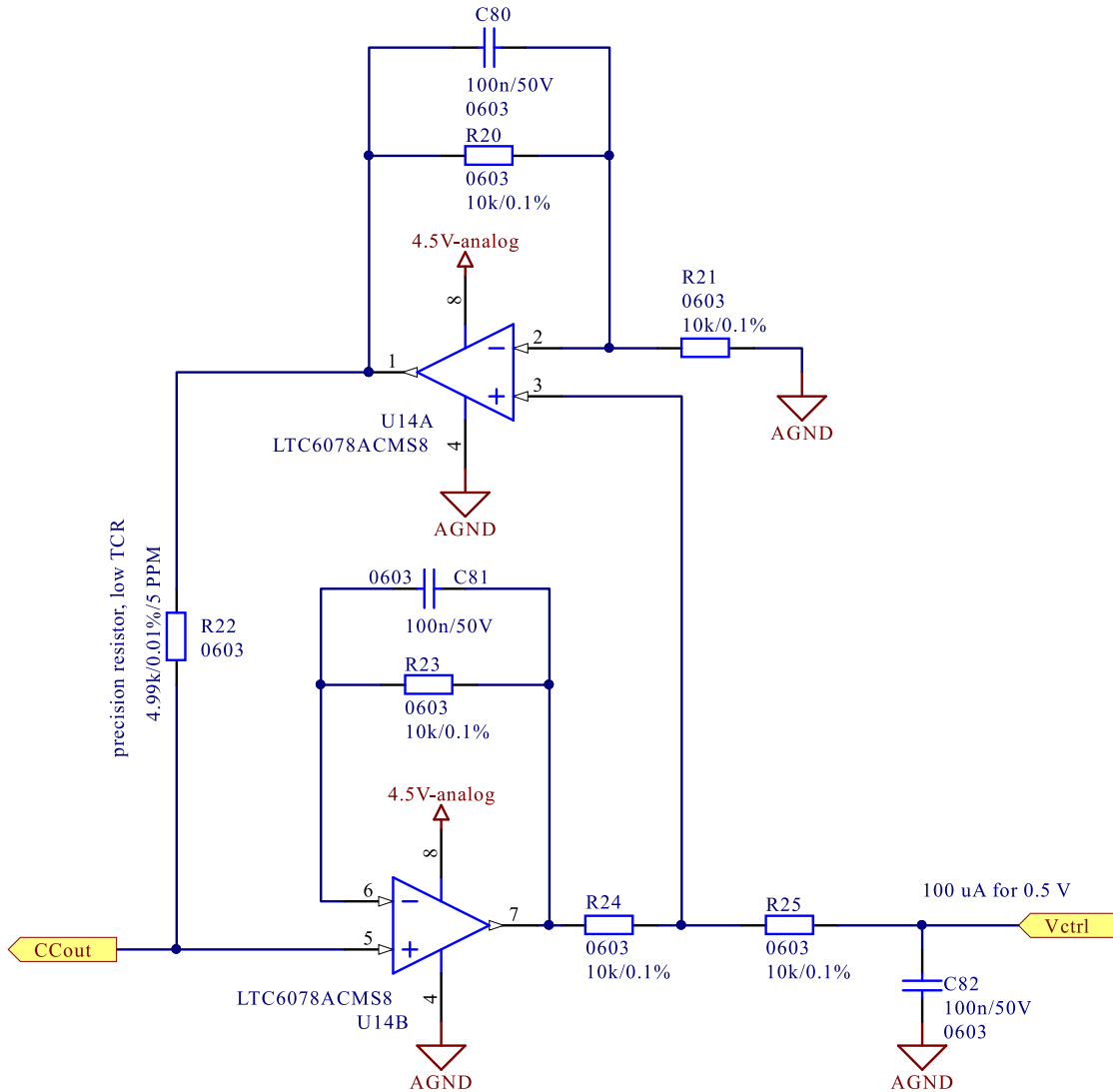


Figure 5.6: Schematic of voltage-controlled current source.

### Resistive Thermal Devices - PT1000 Platinum Sensors

Platinum resistive sensors are widely used in precise temperature measurements in a wide range. RTD is a passive device whose resistance increases with increasing temperature with a well-defined characteristic. [24] Usable temperature ranges and resistance-temperature conversion formulas for platinum sensors are specified by IEC751 / ITS-90 standards. Since platinum RTDs are solely metallic devices, they can be placed close to the irradiated transistors.

From a point of view of readout circuit, measurement of the temperature by a RTDs involves a precise resistance determination.[24] Because of relatively low sensitivity (about  $+4 \Omega/\text{ }^\circ\text{C}$  for PT1000), special care must be paid to minimize influence of long cables, tracks on PCB or sockets that may introduce additional resistance, sometimes varying in time. Widely used approach involved four terminal measurement, also referred as Kelvin sensing, which separates current and voltage paths. A schematic diagram of the system is presented in Figure 5.8. A RTD is biased by a constant current source, while a voltage drop across the RTD is measured by a differential amplifier with high-impedance inputs. Since almost no current flows through voltage-sense wires, so the influence of  $R_L$  is negligible.

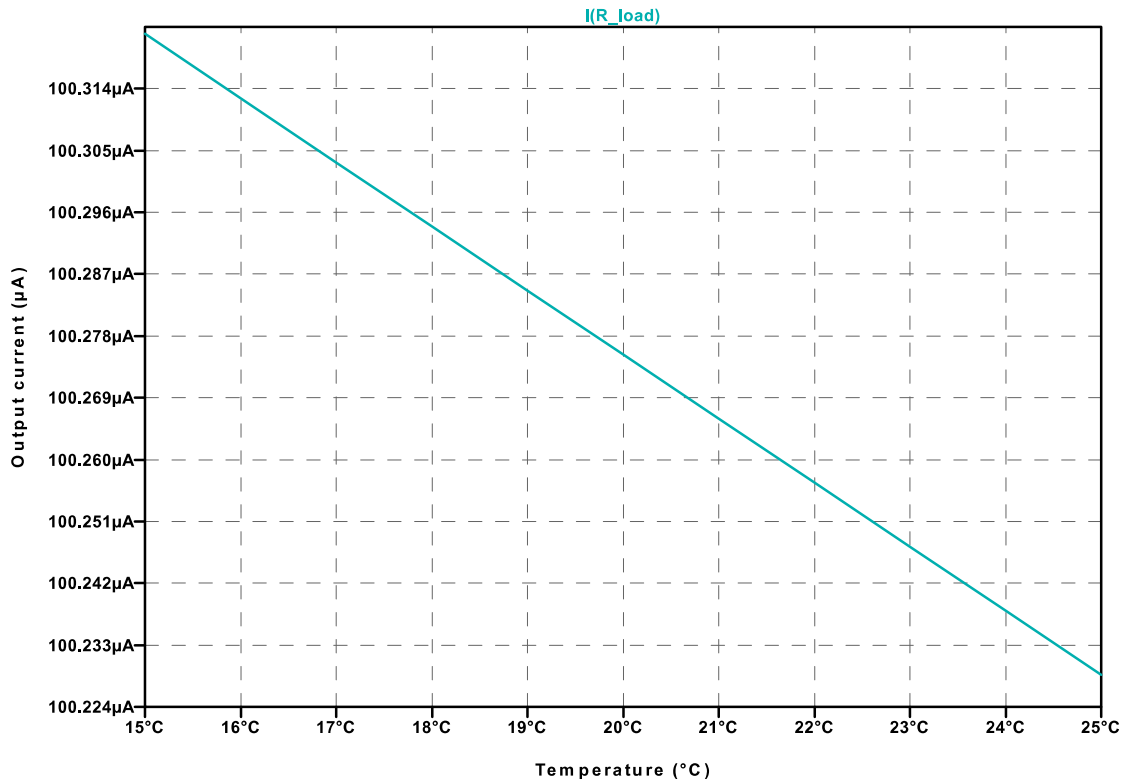


Figure 5.7: Output current temperature dependence simulation.

Resistance of the RTD is described by Eq. 5.1.

$$R_{RTD} = V_{out}/I \quad (5.1)$$

where:

$R_{RTD}$  - resistance of the RTD

$V_{out}$  - output voltage from differential amplifier

$I$  - current from constant current source

Current flowing through RTD dissipates energy on it, heating-up the device. To minimize the effect, called self-heating, the excitation current should be limited in value.[24]

As the RTD fulfilling requirements for the project, a platinum PT1000 sensor in small, surface mounted package 0805 was chosen (Figure 5.9).

Since RTDs are purely analog devices, apart from biasing circuit and differential amplifier, they need an analog-to-digital converter circuitry, especially to cooperate with a digital world of microprocessors. To simplify the biasing and readout circuits, a single integrated circuit was chosen to interface the RTD directly to the microcontroller. A MAX31865 from Maxim Integrated [27], resistance-to-digital converter was used. Table 5.2 summarises the most important parameters of the integrated circuit.

Taking into account long wires between a readout circuit and the RTD sensors, in order to enhance noise performance of the circuit, additional common-mode and differential-mode filters were added at differential voltage sensing inputs of MAX31865.[14] The actual schematic of the readout circuit is shown in Figure 5.10.

Since the reference voltage for internal ADC in MAX31865 is produced by a current flowing through an external, reference resistor ( $R_{19}$  in Figure 5.10), it was chosen taking a special care. A precise resistor with

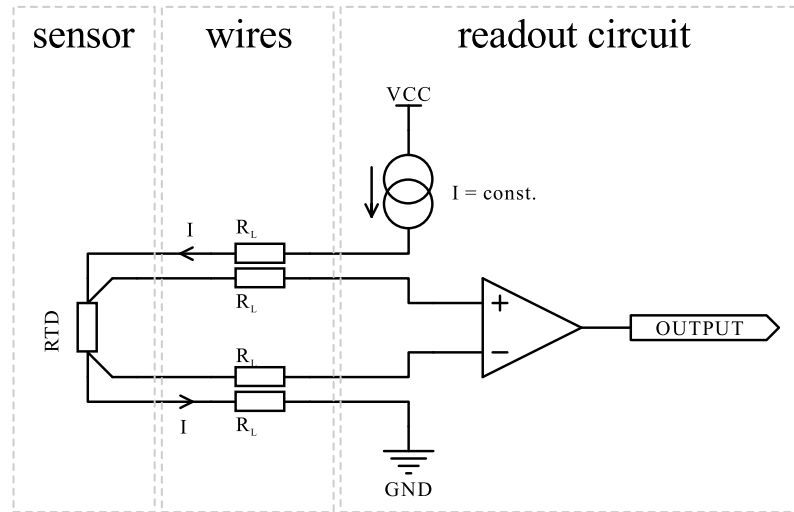


Figure 5.8: A block diagram of four wire measurement technique.

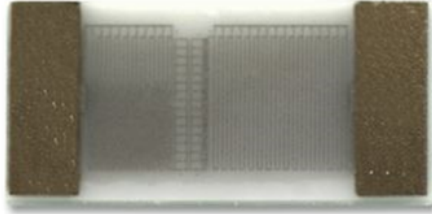


Figure 5.9: Resistive thermal device PT1000 in SMD 0805 package. [38]

resistance of  $4.99 \text{ k}\Omega$  and tolerance of 0.01% with a low temperature coefficient  $5 \text{ ppm}/^\circ\text{C}$  from ARCOL / Ohmite was selected, making a reference voltage initially accurate and minimizing changes caused by a temperature shifts.

### LM60 Integrated Temperature Sensors

If properly handled, RTDs give a high precision temperature readout. In order improve reliability of measurements and provide redundancy to the system, another supporting thermometers were added. For this purpose precision integrated-circuit temperature sensors LM60 from Texas Instruments were selected.[26] The output voltage of the sensors is linearly proportional to the temperature with a DC offset - see Eq. 5.2.[26]

$$V_{out} = T_{sens} \cdot 6.25 [\text{mV}/^\circ\text{C}] + 424 [\text{mV}] \quad (5.2)$$

where:

$V_{out}$  - output voltage from the sensor [mV]

$T_{sens}$  - temperature of the sensor [°C]

An analog signal from the sensor is converted by built-in AVR microcontroller 10-bit analog-to-digital converter. Reference voltage for the converter has a value of 1.8 V. It yields a  $0.3 \text{ }^\circ\text{C}/\text{LSB}$  resolution, but might be enhanced by an oversampling technique.[9] Since temperature is a quantity that changes relatively slowly, averaging of many samples is possible and used in the system.

Table 5.2: Basic specification of Maxim Integrated MAX31865 resistance-to-digital converter.

Supported RTDs	PT100 to PT1000
4-wire configuration	✓
ADC resolution	15 bit
Built-in RTD's bias	✓
Temperature resolution	0.03125 °C
Total Accuracy	better than 0.5 °C
Digital interface	SPI-Compatible
Supply voltage	3.0 - 3.6 V

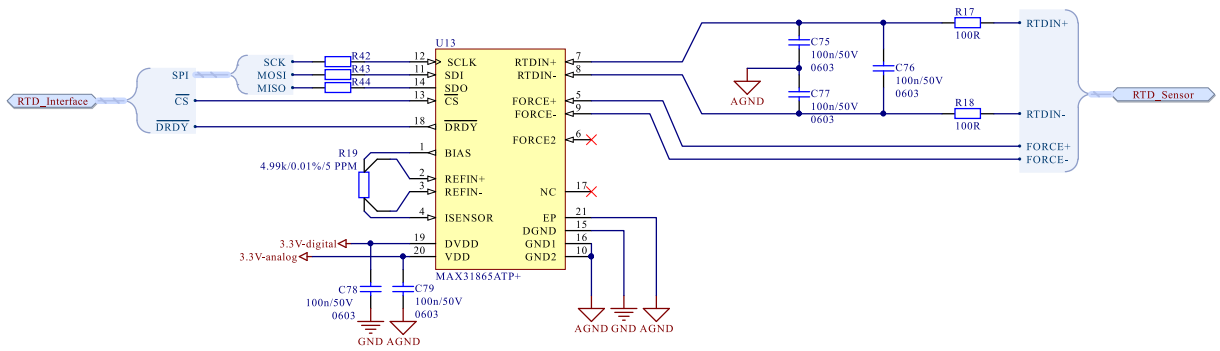


Figure 5.10: A schematic of RTD readout circuit.

### 5.3.3. Microcontroller unit

The main microcontroller in the calibration stand is responsible for communication with an operator (receiving and interpreting commands, returning results), acts as a master in communication with other integrated circuits on board (i.e. ADC AD7714YRZ, DAC1220E, RTD interface MAX31865ATP+), controls I/O lines for multiplexers and measures analog voltages. Since the processing of acquired data takes place at a client side (i.e. PC software), a computational power is not a key point in selection process. Because of popularity, well-known architecture, rich set of peripherals and proven reliability in a harsh, radiation environment [3] Atmel's AVR ATMega family was taken into consideration. Table 5.3 summarises requirements defined by the rest of the circuit. As the model fulfilling specified requirements, an ATMega128A in a TQFP-64 package was chosen.

Table 5.3: Requirements for the microcontroller.

I/O lines	25
SPI	1
UART	2
ADC	2 channels
Programming & debugging	JTAG
Power supply	3.3 V

The MCU is clocked with a signal generated by a 11.0592 MHz crystal, to ensure stability, that is needed especially for an asynchronous UART communication. The microcontroller is powered from a stabilized 3.3 V shared with other digital circuits. However, in order to improve performance of internal ADC converter, an external source of 1.8 V reference voltage was used. The way of connection can be seen in Figure 5.11.

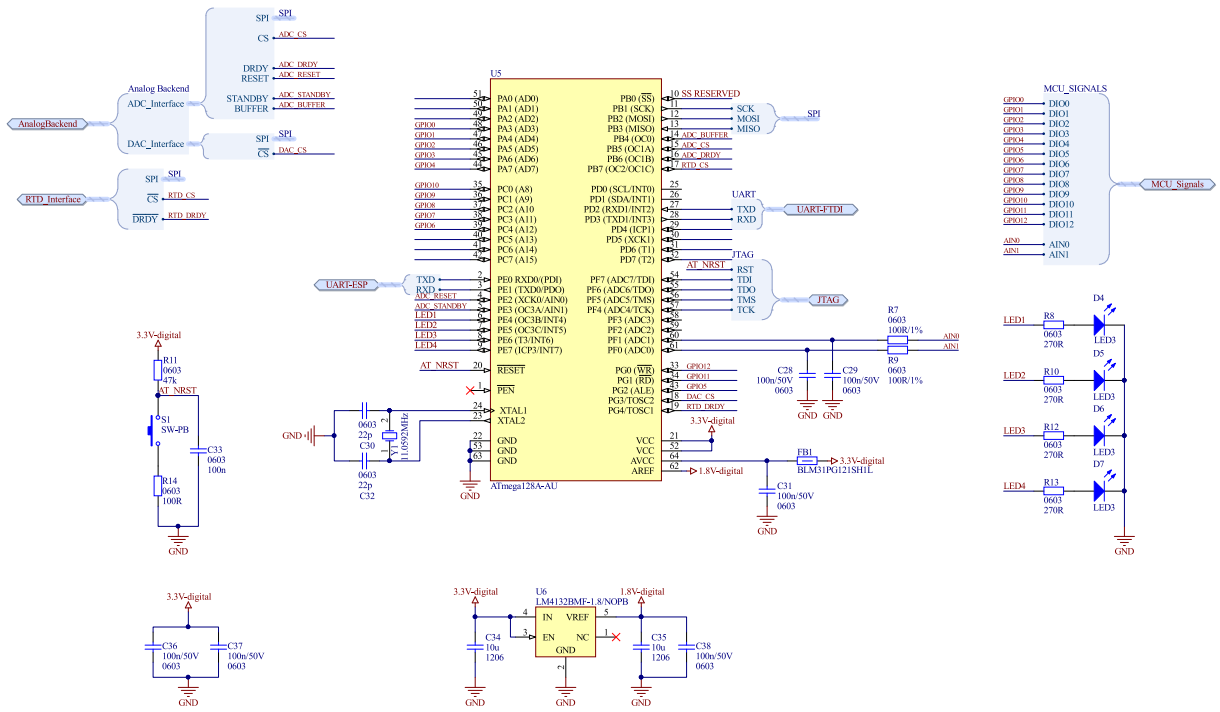


Figure 5.11: A schematic of MCU circuit.

### 5.3.4. Communication interfaces

The calibration stand is equipped with two types of communication interfaces: wired and wireless. Wired connection is a convenient option when the stand is located close to a computer (e.g. during testing or temperature calibrations), whereas wireless connection is meant to be used during TID calibrations.

### Wired UART connection

Wired communication is realized by FT231 - UART to USB interface from FTDI [31]. USB Type B socket was chosen due to its robustness and availability of long USB A-B cables (up to 5 m), making the operation with a stand more convenient. Data transmission is indicated by two LEDs - one for transmit and receive events. A schematic is shown in Figure 5.12.

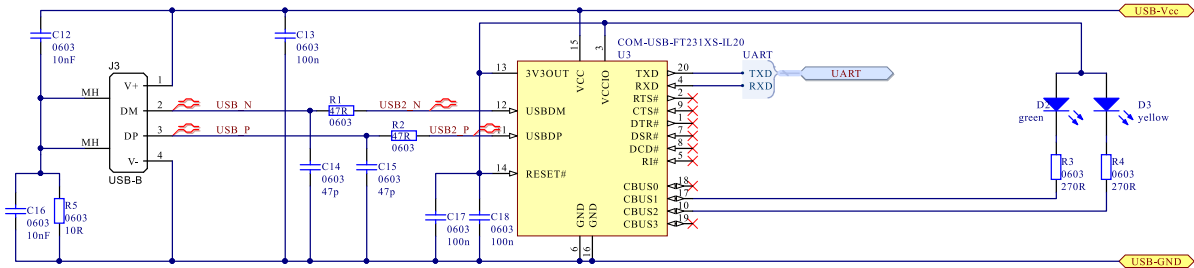


Figure 5.12: Connection of FTDI USB to UART interface.

The computers contain abundant noise sources, only to mention switching power supplies and fast digital signals buses, generating noise in a broad spectrum of frequencies. Taking into account significant noise amount that would be injected to the measurement system from a PC by a direct connection, a galvanic isolation was utilized. The isolation comprises optocouplers (ACPL-K63L) located between FTDI chip and MCU's UART interface pins (RX, TX). Isolated side is powered by a voltage from USB port.

### Wireless WiFi network connection

Wireless communication of the stand with a PC computer was accomplished utilizing IEEE 802.11-compliant WLAN network. Such a choice reduces number of demanded hardware (WLAN cards are typically built in a notebook computers) and allows to extend a range of the signal in affordable and low-cost way. From the point of view of on-board microcontroller, Atmel's ATmega128A, a communication via 2.4 GHz WiFi network has no differences comparing to a standard, wired UART connection. It was possible by utilization of a module with Espressif's ESP8266 WiFi SoC[17], programmed to act as bidirectional WiFi to UART bridge.

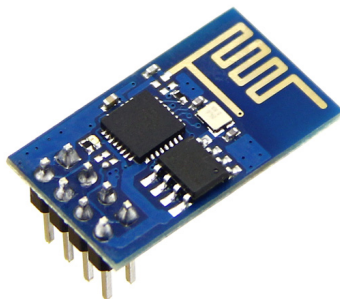


Figure 5.13: A module with ESP8266 WiFi SoC. [23]

The ESP8266 SoC offers complete and self-contained WiFi capabilities. It integrates antenna switches, RF balun, power amplifier, low noise receive amplifier, filters and power management modules. [17] Selected module

ESP-01 (see Figure 5.13) comprises 4 Mb flash memory to store an application code, a 26 MHz crystal and meander-line antenna. Power supply pins and ESP8266's GPIOs (UART, digital I/O, reset) are available through a standard 2.54 mm pitch 4x2 header connector. Thanks to the bootloader, flashing of a new firmware might be carried out via UART interface.

The ESP8266 can be powered from 3.0 - 3.6 V source, with a peak current consumption up to 170 mA.[17]. Due to possibility of spoiling noise performance of analog part of the calibration stand the ESP8266 module is powered from external power supply (or USB port) through a LMS8117A low-dropout linear regulator. The UART interface between the ESP8266 and the AVR MCU is opto-coupled (but a ground is common with USB ground).

### 5.3.5. Power supply

In all mixed-signal circuits, a power supply plays a key role. Its not only intended to deliver proper voltage levels for different parts of the circuit, according to their specification but the power supply design and its quality have a significant reflection in the circuit's noise performance. General assumption is that the calibration stand should be powered by the two independent voltage sources. The first, the main (6 - 12 V @ 100 mA) is intended to deliver power for all circuits but communication interfaces which are galvanically isolated (the ESP8266 and FTDI UART-USB converter). The power supply of communication part is delivered directly by the USB port - for the FTDI, whereas for the ESP8266 there are two possibilities - by a 4 - 12 V @ 400 mA voltage source or USB port – see Fig. 5.14.

The main part of the circuit can be supplied from a stabilized, DC power supply or a battery. To prevent from circuit damage in the event of wrong connection to the power supply, a reverse polarity protection was implemented. The solution consists of a single, high-side P-MOSFET transistor placed in the power path. [25] Then, an input capacitors along with a common-mode choke were placed to suppress a noise coming from the power supply. Preliminary filtered voltage is fed to a few low-dropout voltage linear regulators supplying particular parts of the circuit, as shown in Figures 5.14 and 5.15. All parts in the circuit can be classified as digital, analog or mixed-signal with separated digital and analog supply. Therefore, separate LDOs are dedicated for analog and digital parts of the circuit. The LDOs' high power supply rejection ratio in a wide range of frequencies prevent from noise sharing. Additionally, the digital and analog grounds were distinguished in order to separate return current paths from analog and digital circuits.

### 5.3.6. Printed circuit boards design

Printed circuit board were designed in Altium Designer EDA software. All library components were prepared with 3D models, allowing for better placement and board planning. The two-layer PCBs were optimized to meet expectations for good noise performance of the calibration stand. Digital and analog parts of the circuit were grouped together. Furthermore, analog and digital grounds were separated and tied together at one point to separate return paths for currents from analog and digital parts in order to minimize errors in a ground voltage level.[21] Linear voltage regulators were placed close to the parts of the circuit that are supplied with them to avoid long paths. A similar policy was applied to a voltage references' placement. The high-speed digital lines and GPIOs from the microcontroller were routed in the groups and shielded by the ground planes. Susceptible to noise analog

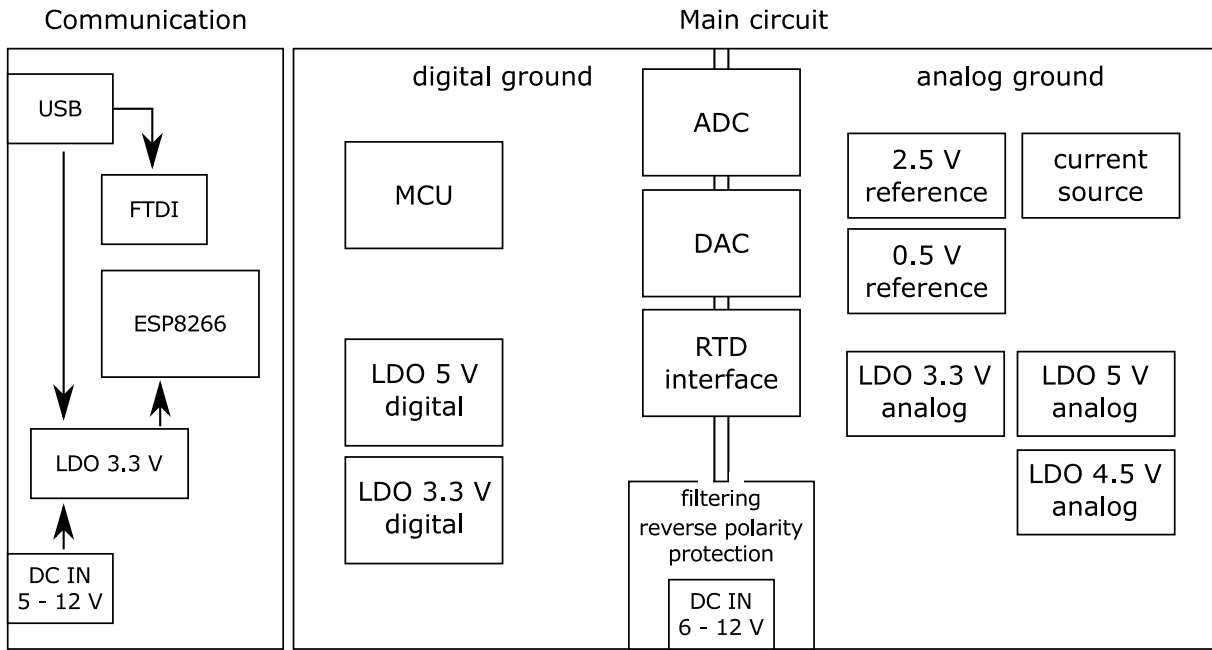


Figure 5.14: A block diagram of the power supply along with device classification (analog/digital/mixed-signal).

lines in the IDC-40 socket were grouped together and separated by the grounded wires. The layouts of designed printed circuit boards are presented in Figures 5.16 - 5.19, whereas Figures 5.20 and 5.21 show 3D renders of the circuits with the components.

## 5.4. Software design

### 5.4.1. Embedded software for AVR MCU

The software for the ATmega128A microcontroller was written in C++14 programming language and compiled by the avr-g++ compiler. A modern version of C++ language provides an object-oriented programming paradigm, namespaces, templates, new data types, constant expressions (`constexpr`) allowing to write well-organized, clean and efficient code. The application code utilizes the AVR-HAL library. The AVR-HAL is a set of drivers providing an abstraction layer for peripherals of the AVR microcontrollers family. The drivers for external devices (e.g. MAX31865ATP+, AD7714, DAC1220, ADG708) were written utilizing low-level functions from the AVR-HAL library. The diagram in Figure 5.22 shows an organization of the software.

The stand recognizes commands summarized in Table 5.4. The commands sent by both USB and TCP/IP are the same. Commands from both interfaces are parsed in the UART RX interrupt handler and then they are appended into common task queue. The main thread of the software executes the tasks stored in the queue one by one and sends the results by both communication interfaces. Such solution allows to send multiple commands describing specific measurement scenario and wait for the reply.

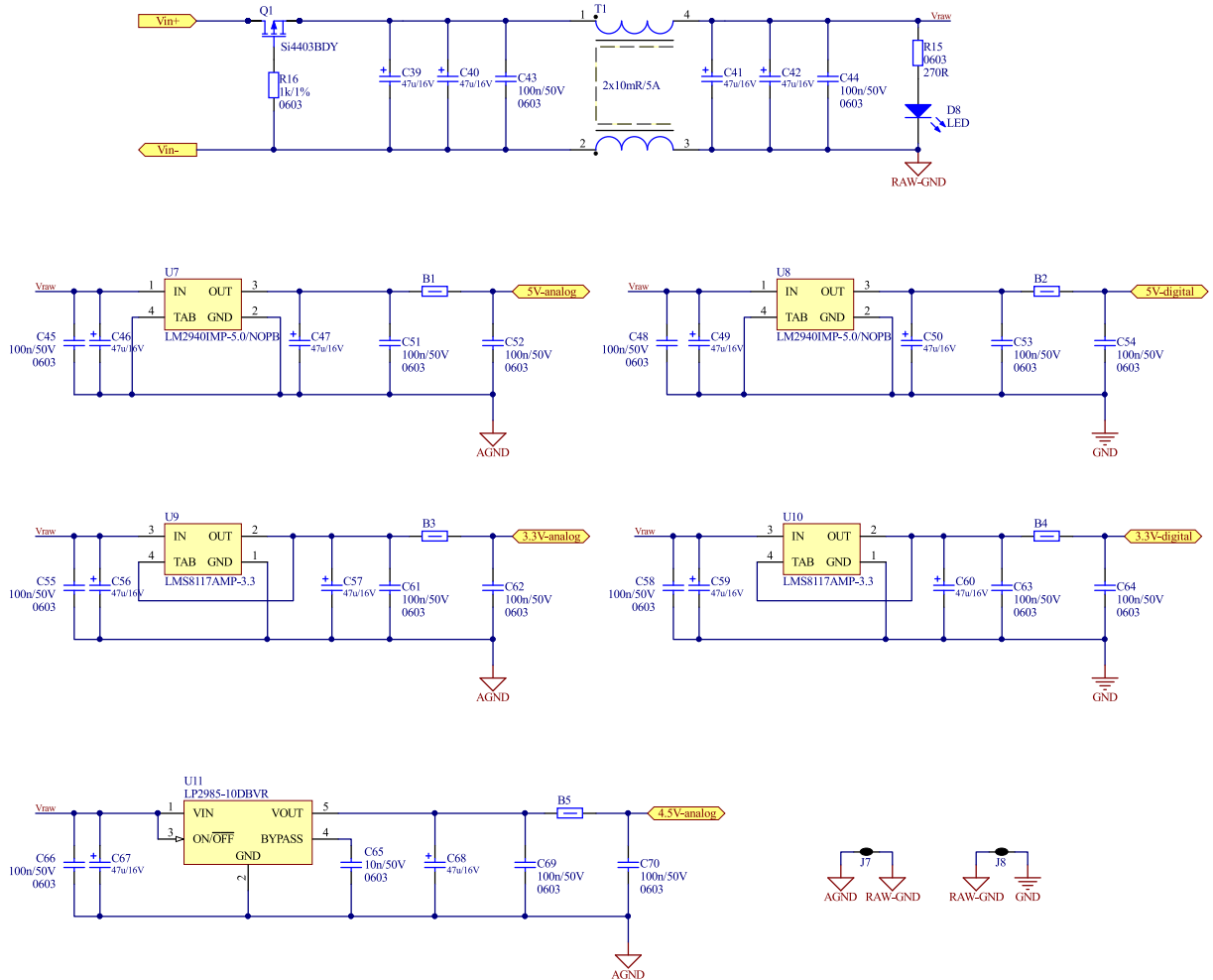


Figure 5.15: A schematic of main power supply circuit.

#### **5.4.2. Embedded software for ESP8266 MCU**

The ESP8266 is programmed in a way that it acts as a bidirectional UART - TCP/IP bridge. It connects to a specified WiFi network, authenticating with a provided WEP password. In case of failure, the attempt is repeated several times and then the chip tries to restart itself. Once the connection with the WiFi network is established and the ESP8266 successfully obtained an IP address from DHCP server, it starts a TCP server and listens for a client on a specified port. When the client's IP address is known, the exchange of data can take place. When a TCP packet is received, its content is send via UART. Similarly, when UART input (RX) buffer is not empty, the data are transferred to the client by a TCP packet.

The software is written with the Wiring hardware abstraction layer library port for the ESP8266 MCU.

### **5.4.3. PC control software for the stand**

Although, the communication protocol and commands were designed to allow for manual operation using ordinary serial port terminal, for on-line measurements a software with graphical user interface was prepared. The

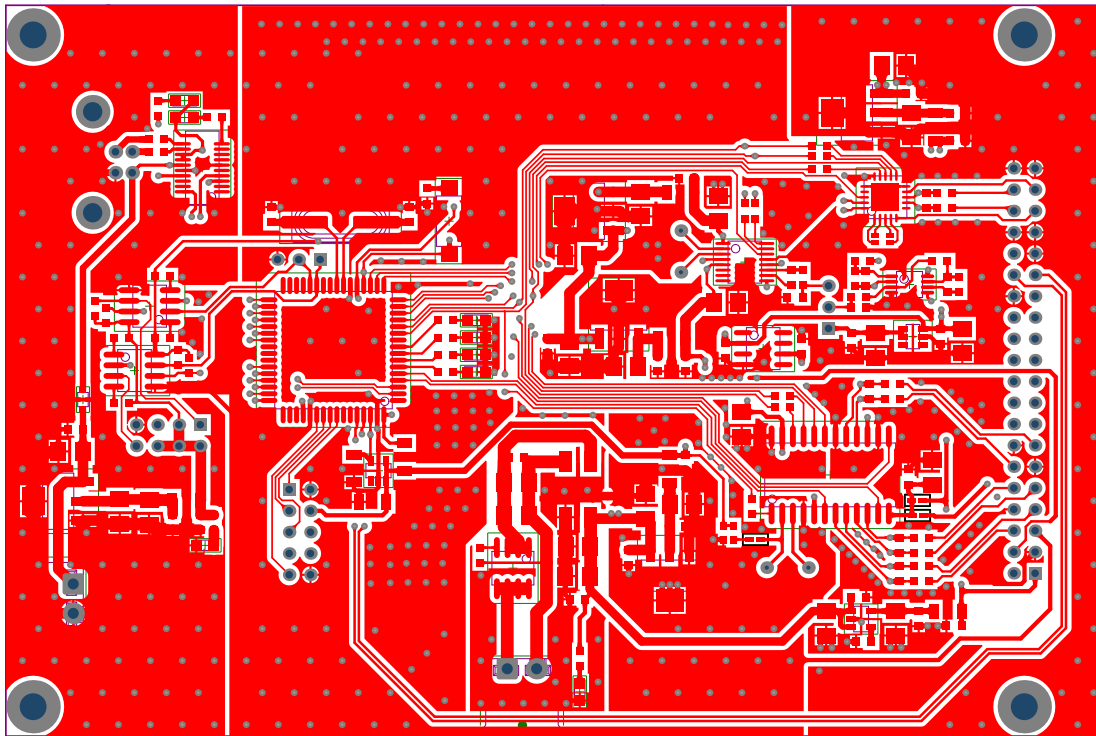


Figure 5.16: Top layer of designed main PCB.

control panel was created in NI LabVIEW environment. Architecture of the application is based on queued state machine and consumer/producer design patterns. The application has several options: communication with stand via UART or TCP/IP, temperature calibrations,  $I_{ZTC}$  measurements, TID calibration, I-V curve determination and free-running and manual modes – see Fig. 5.23.

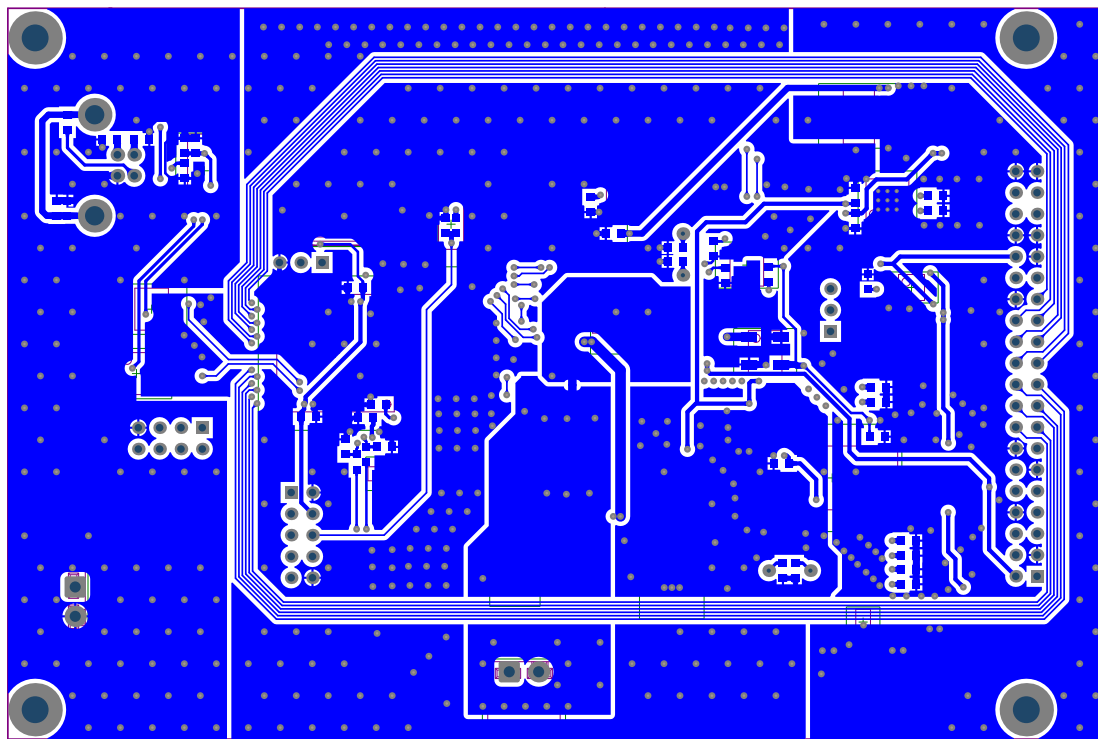


Figure 5.17: Bottom layer of designed main PCB.

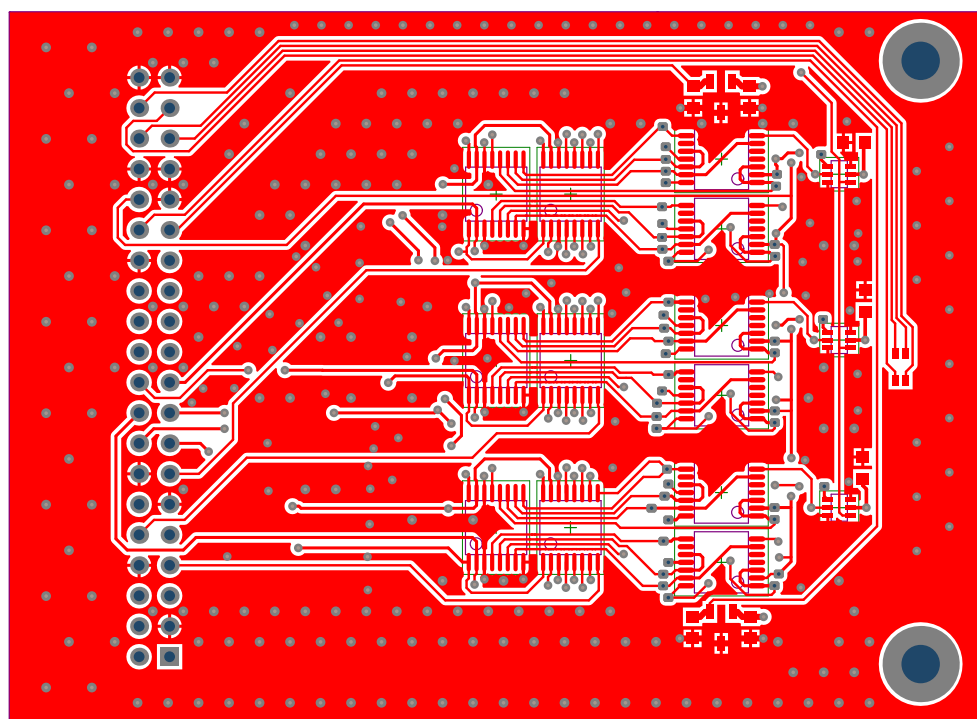


Figure 5.18: Top layer of designed card PCB.

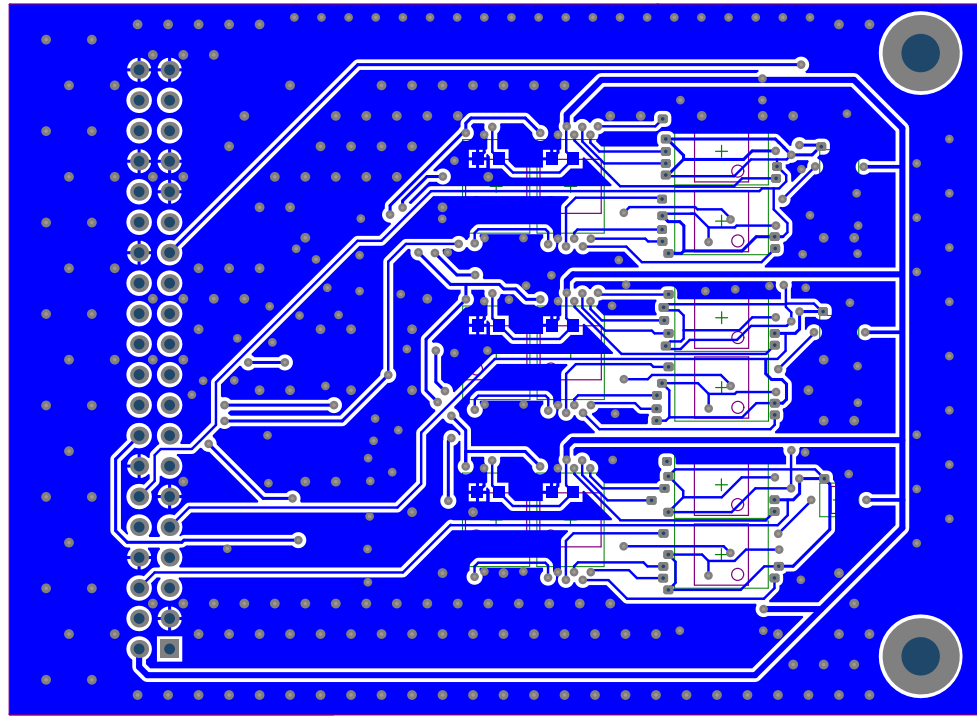


Figure 5.19: Bottom layer of designed card PCB.

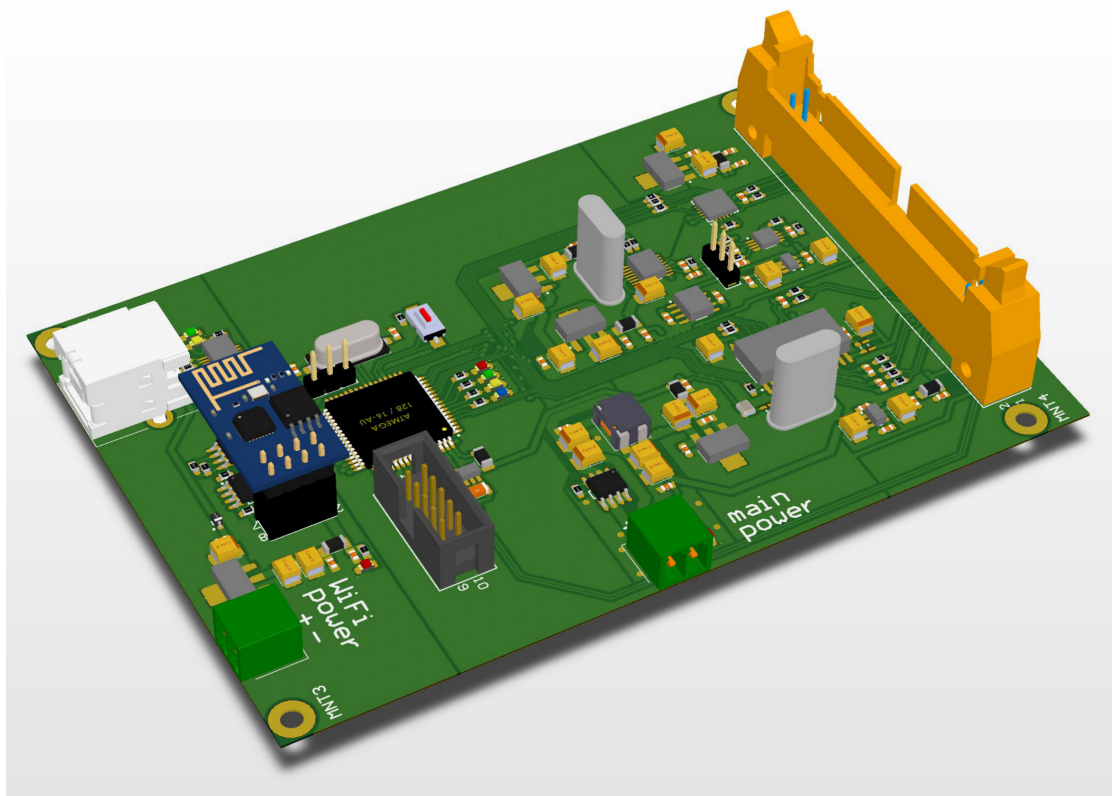


Figure 5.20: 3D view of designed main PCB.

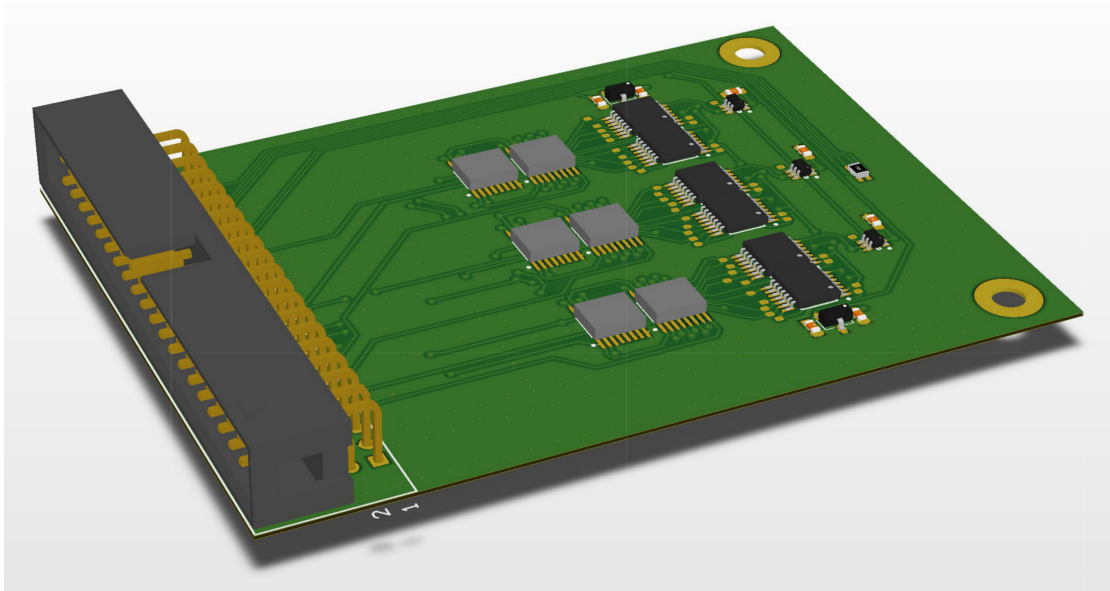


Figure 5.21: 3D view of designed card PCB.

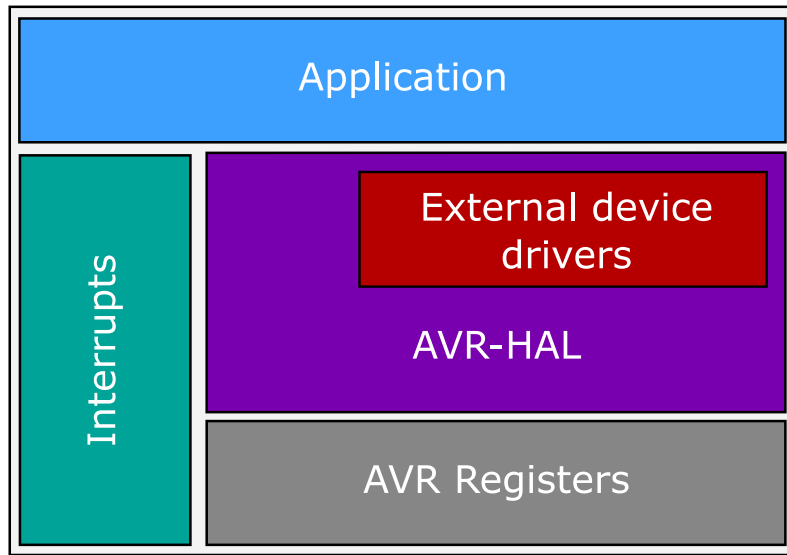


Figure 5.22: AVR software architecture.

Table 5.4: The summary of all available commands.

Description	Command	Reply
<b>Measure threshold voltage</b> [CH] = 0 ... 17 [RAW] = raw reading from 24-bit ADC	MOS [CH]	MOS [CH] [RAW]
<b>Measure diode forward voltage</b> [CH] = 0 ... 5 [RAW] = raw reading from 24-bit ADC	DIODE [CH]	DIODE [CH] [RAW]
<b>Measure reference RTD temperature</b> [RAW] = raw reading from RTD interface	RTD	RTD [RAW]
<b>Measure reference LM60 temperature</b> [CH] = 0 ... 1 [RAW] = raw reading from 10 bit AVR's ADC x 16 (oversampled)	LM [CH]	LM [CH] [RAW]
<b>Set constant current source value</b> [VAL] = 0 ... 900000 (nA)	SETCC [VAL]	SETCC [VAL]
<b>Turn off constant current source</b>	CCOFF	CCOFF
<b>Reset all tasks in the queue</b>	RESET	RESET

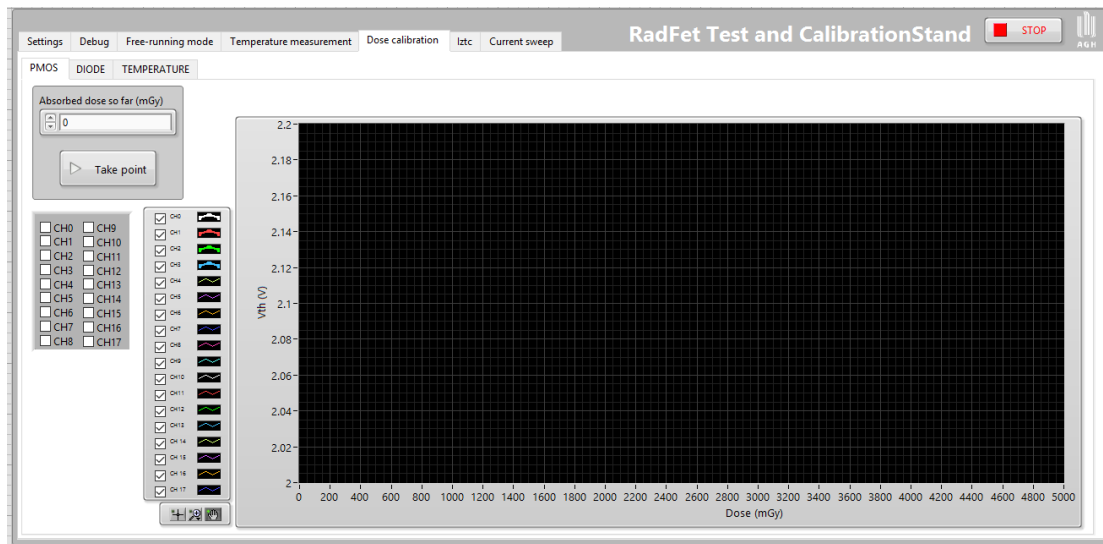


Figure 5.23: LabVIEW control panel.

## 6. Test and calibration stand performance

In this chapter can be treated as a commissioning report for the test and calibration stand. Moreover, a basic characterisation of the stand performance is presented, followed by the results of carried out preliminary extractions of desired parameters of the CD4007 IC.

### 6.1. Current source characteristics

At first, the measurements were carried out for the current source with controlling signal from a voltage reference. Output current was measured by an Agilent HP34970A data acquisition unit. Mean value of the current source working in a fixed mode is  $99.81 \mu A$  with  $\sigma = 0.053 \mu A$  – Fig. 6.1. These measurements confirm that the circuit fulfils design assumptions. Next part under commissioning was an adjustable constant current source. In this case, the most important test is a correlation between set current via communication interface and actual output current. Obtained curve is shown in Fig. 6.2. The results show significant offset and gain errors, however once the transfer characteristic is known, correction coefficients can be uploaded to AVR software improving the CCS performance.

The changes in output current due to temperature variations have been also specified. Figure 6.3 shows temperature tests of the current source working in a fixed or adjustable modes. Measurement was based on heating-up of the whole main board – Fig. 6.3. The CCS in a fixed mode exhibits practically no temperature dependence in a range of interest, whereas changes in adjustable mode are affordable.

### 6.2. P-MOSFET characterisation

#### 6.2.1. I-V characteristic

The operating point of P-MOSFET transistor should be chosen so that the ADC input range is sufficient for desired TID and temperature variations. The I-V characteristic is shown in Figure 6.5.

#### 6.2.2. Threshold voltage noise measurement

Noise and stability tests were prepared in order to figure out how accurate  $V_{Th}$  determination can be achieved. During the acquisition of 250 samples of  $V_{Th}$  the CD4007 ICs were kept in a constant temperature. The results are presented in Fig. 6.6. Statistical analysis yields distribution close to normal (, with  $\sigma = 15 nV$  – see Fig. 6.7.

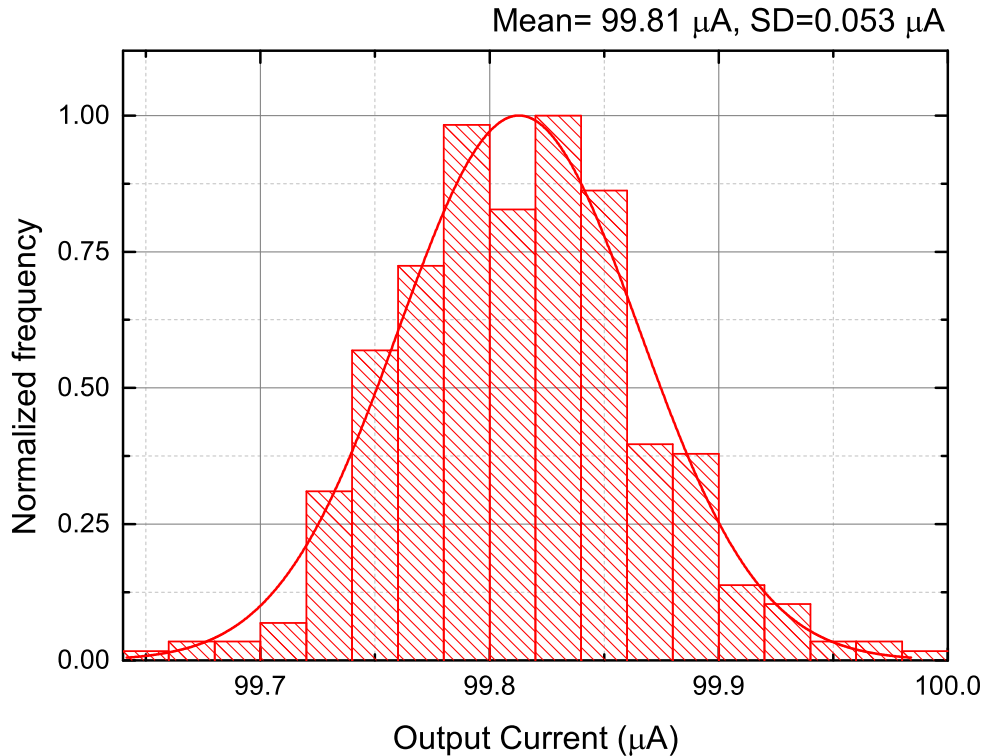


Figure 6.1: Noise statistical analysis of the constant current source.

### 6.2.3. Temperature calibration

Tests of temperature compensation for  $V_{Th}$  changes were performed. At first, extraction of temperature coefficients for transistors biased with an arbitrary chosen constant current of  $99.8 \mu A$ . The main aim of the test was to check linearity of  $V_{Th}(T)$  dependence and temperature coefficient variations among individuals. Plotted dependence is shown in Figure 6.8, whereas extracted coefficients with an average value and standard deviation are up in the Table 6.1. The results show a high linearity and reproducibility.

Another type of thermal measurement was carried out in order to estimate the  $I_{ZTC}$  current, i.e. a current at which temperature dependence is minimal. Collective measurement data are shown in Figure 6.9, whereas for extracted temperature coefficients at each biasing current see Figure 6.10. The  $I_{ZTC}$  was determined as  $140 \mu A$ .

## 6.3. N-MOSFET body diode characterisation

### 6.3.1. Temperature calibration

During the test a linearity and reproducibility of temperature coefficient (slope) determination were at special concern. Since temperature shifts with respect to some arbitrary reference value rather than the absolute temperature data are important for temperature influence on TID, an intercept value variation can be neglected. Calibration

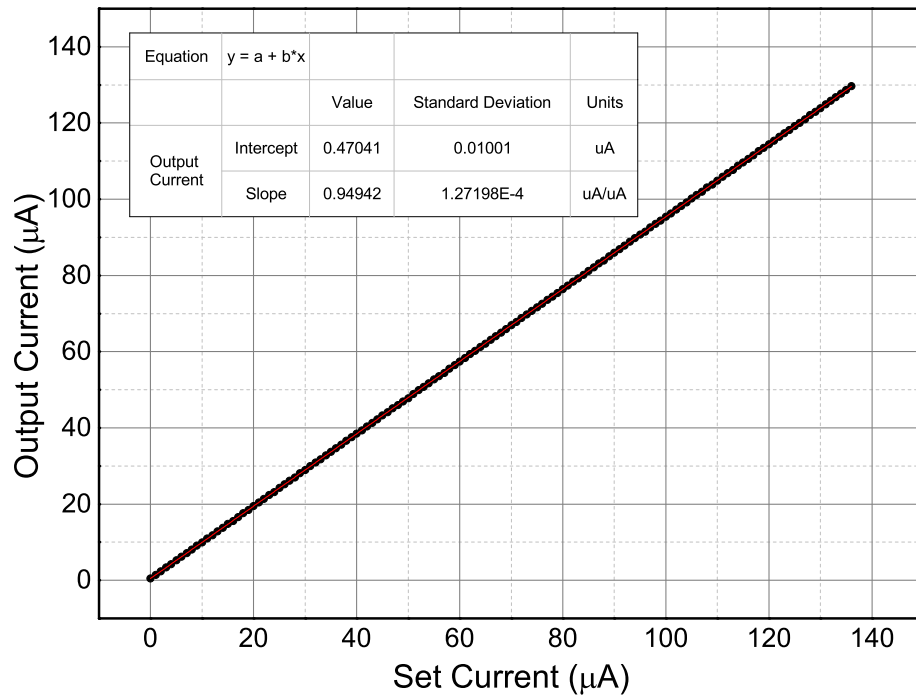


Figure 6.2: Set current vs. output current before calibration at room temperature.

data for temperature measurement using body diode are presented in Figure 6.11 and Table 6.2. The error in temperature measurement carried out by a diode is shown in Figure 6.12. The overall error within specified temperature range does not exceed  $\pm 0.4^\circ\text{C}$ , so the results comply with design assumptions.

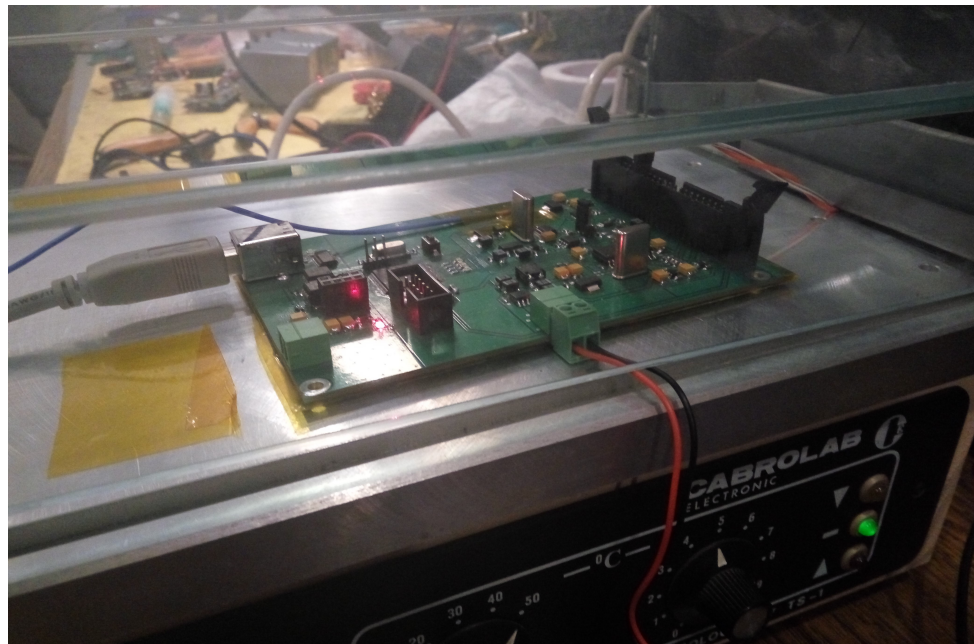


Figure 6.3: Temperature tests of the VCCS.

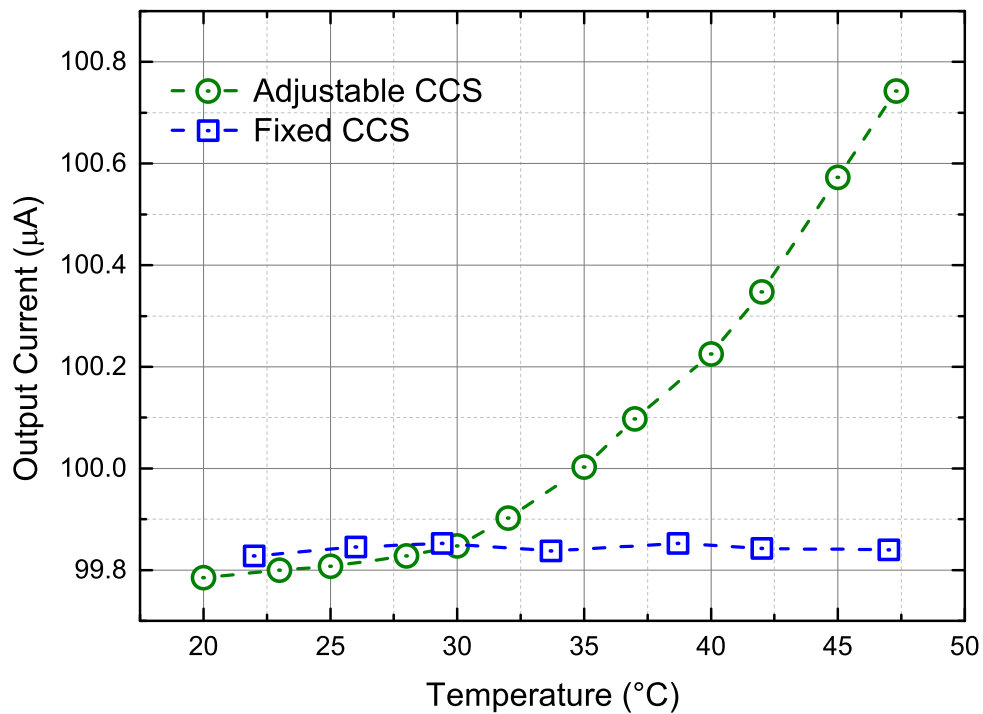


Figure 6.4: Comparison of temperature drift of the CCS in fixed and adjustable modes.

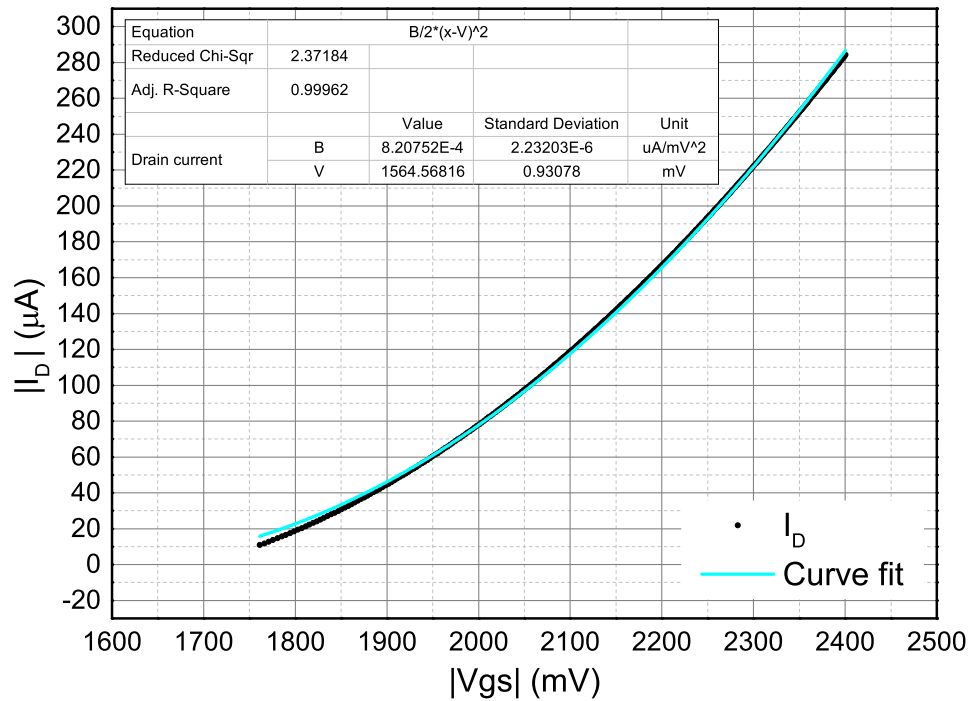
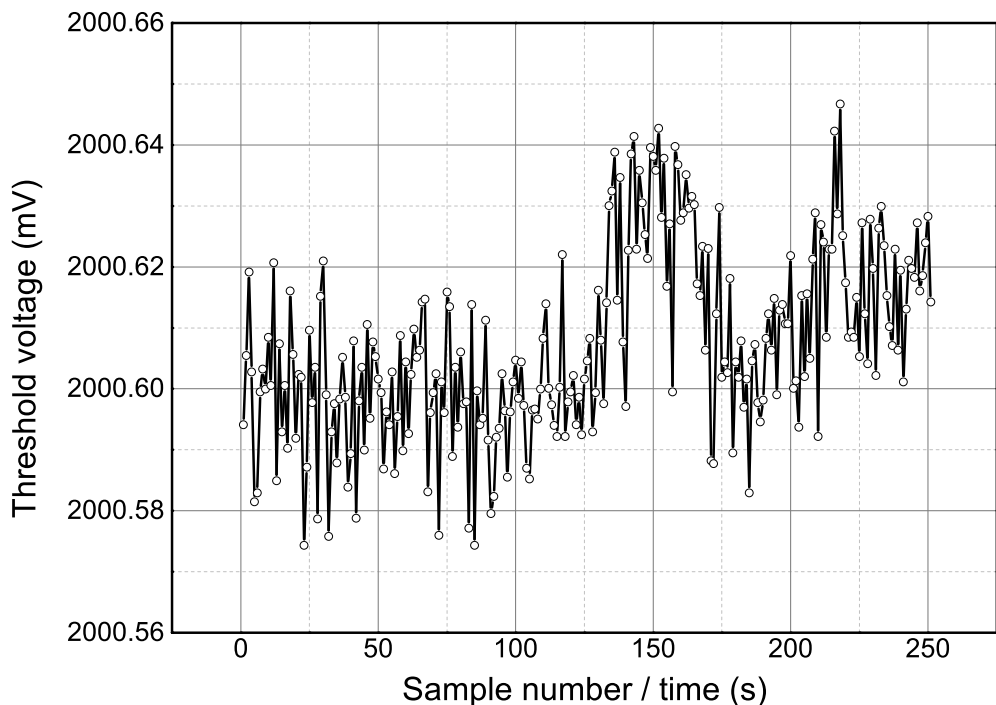
Figure 6.5:  $I_D - V_{gs}$  characteristic of a P-MOSFET from CD4007 IC.

Figure 6.6: Collection of 250 consecutive samples of threshold voltage.

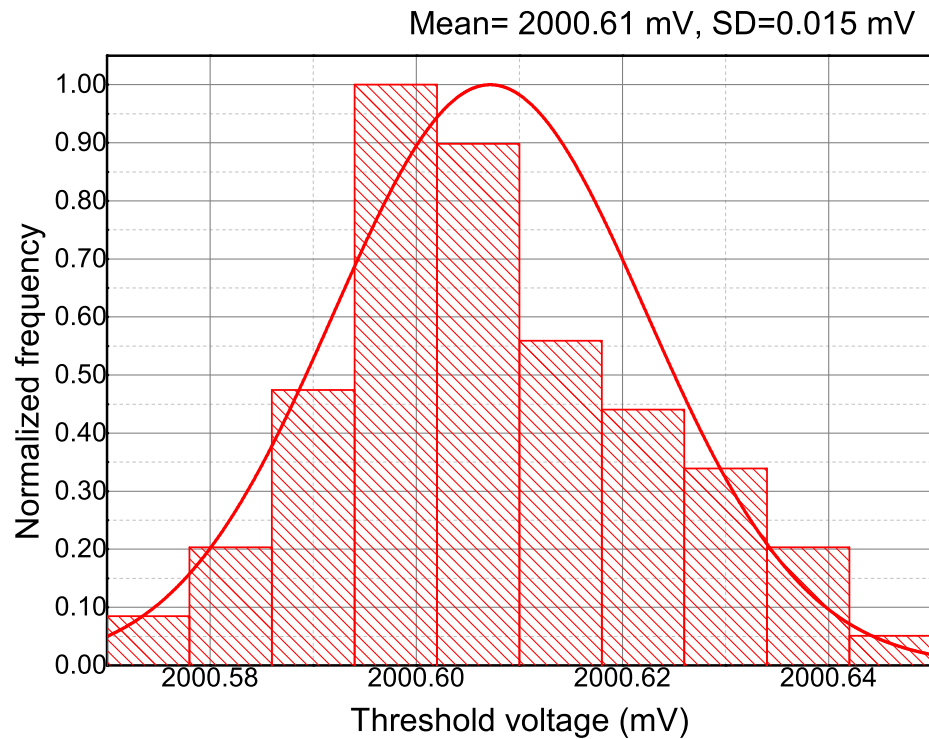
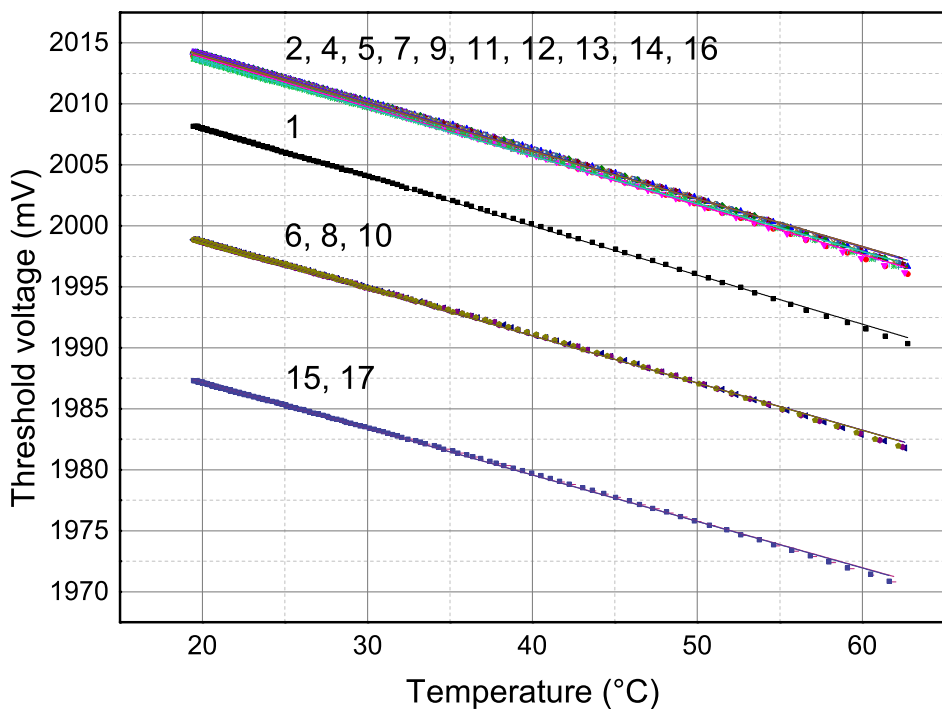
Figure 6.7: Statistical analysis of  $V_{Th}$  samples.Figure 6.8: Temperature characteristic of transistors'  $V_{Th}$  biased by a  $99.8 \mu A$  current (collective plot for 17 transistors, the numbers correspond to those in Table 6.1).

Table 6.1: Temperature coefficients for transistors'  $V_{Th}$  biased by  $99.8 \mu A$  current.

DUT no.	Intercept (mV)		Slope (mV/ $^{\circ}$ C)		Statistics
	Value	Standard Error	Value	Standard Error	Adj. R-Square
1	2016.099	0.02043	-0.40262	6.71E-04	0.99952
2	2021.874	0.01998	-0.4034	6.56E-04	0.99955
3	2022.024	0.02179	-0.39584	7.15E-04	0.99944
4	2021.887	0.01848	-0.40405	6.08E-04	0.99961
5	2022.036	0.02063	-0.3965	6.79E-04	0.9995
6	2006.457	0.02185	-0.38671	7.19E-04	0.99941
7	2022.040	0.02087	-0.39655	6.88E-04	0.99948
8	2006.471	0.02211	-0.38703	7.29E-04	0.99939
9	2021.793	0.02241	-0.39121	7.39E-04	0.99939
10	2006.484	0.02188	-0.38744	7.23E-04	0.9994
11	2021.802	0.02232	-0.39164	7.37E-04	0.99939
12	2021.363	0.02068	-0.39046	6.83E-04	0.99947
13	2021.807	0.02256	-0.39185	7.46E-04	0.99938
14	2021.371	0.02035	-0.39082	6.73E-04	0.99949
15	1994.792	0.01985	-0.38029	6.57E-04	0.99949
16	2021.382	0.02077	-0.39155	6.89E-04	0.99947
17	1994.816	0.02	-0.38116	6.63E-04	0.99948
		Average	<b>-0.392</b>	<b>0.007</b>	

Table 6.2: Analysis of temperature coefficients for body diodes in different CD4007 chips.

DUT no.	Intercept (mV)		Slope (mV/ $^{\circ}$ C)		Statistics
	Value	Standard Error	Value	Standard Error	Adj. R-Square
1	651.5507	0.0641	-2.0397	0.0016	0.99991
2	652.0585	0.0689	-2.0399	0.0017	0.99989
3	652.6968	0.0389	-2.0519	0.0010	0.99997
4	652.2627	0.0444	-2.0464	0.0011	0.99996
		Average	<b>-2.045</b>	<b>0.006</b>	

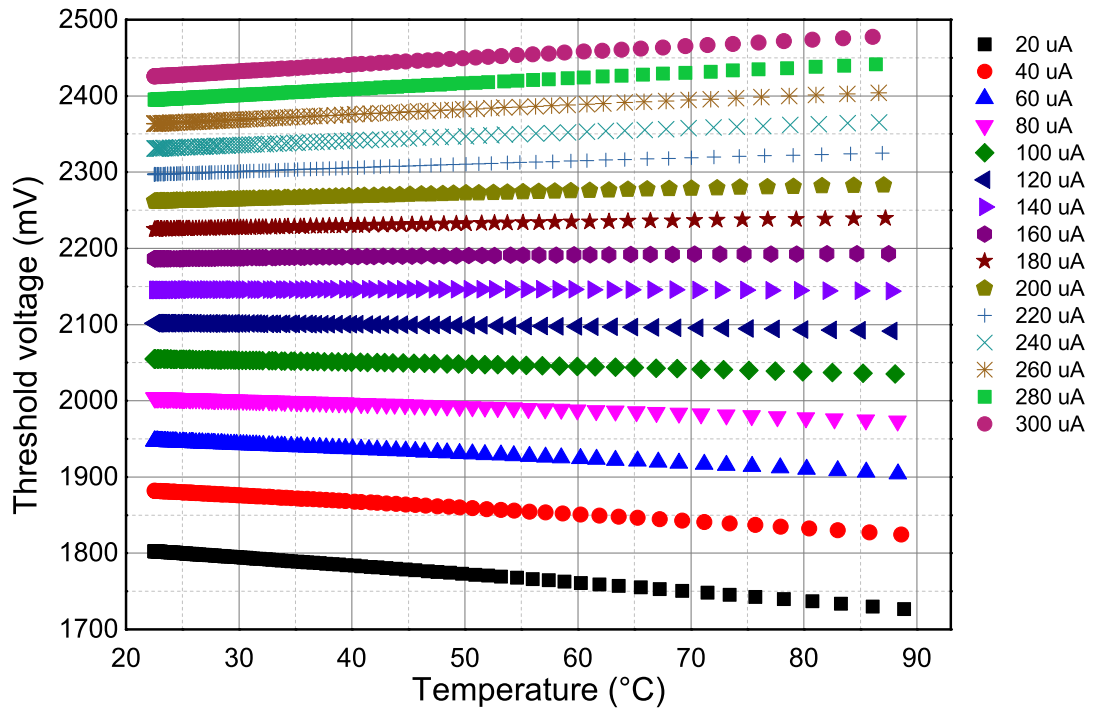


Figure 6.9: Determination of  $I_{ZTC}$  of CD4007 transistor (no. 1 in Tab. 6.1).

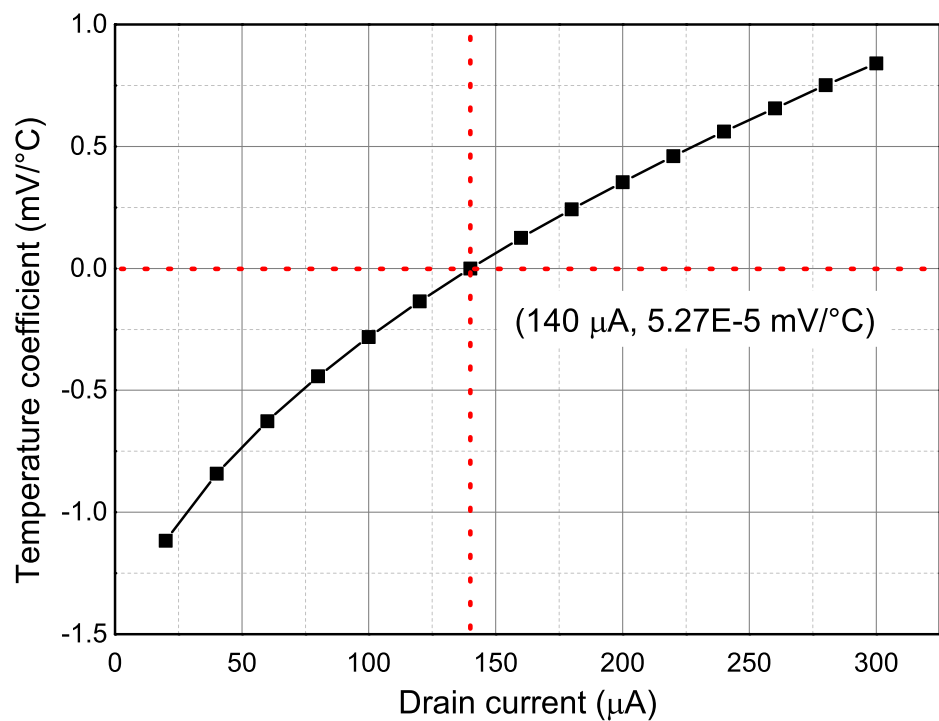


Figure 6.10: Temperature coefficients of transistor no. 1 (Tab. 6.1) for different current bias. Red lines crossing indicates  $I_{ZTC}$  operating point.

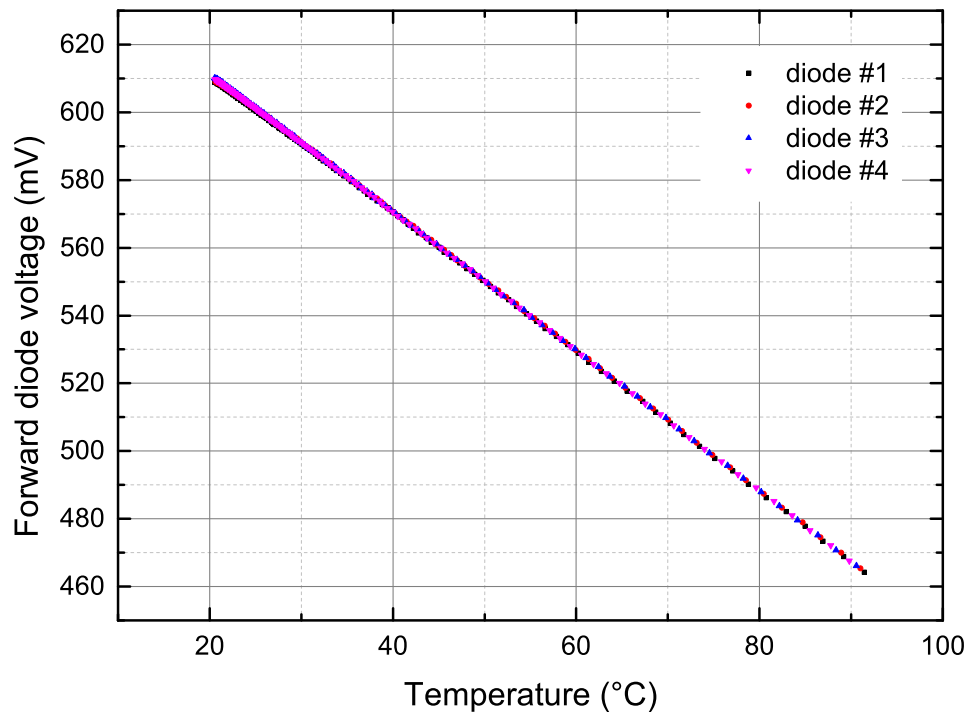


Figure 6.11: Temperature calibration of diodes biased with  $I_f = 99.8\mu A$

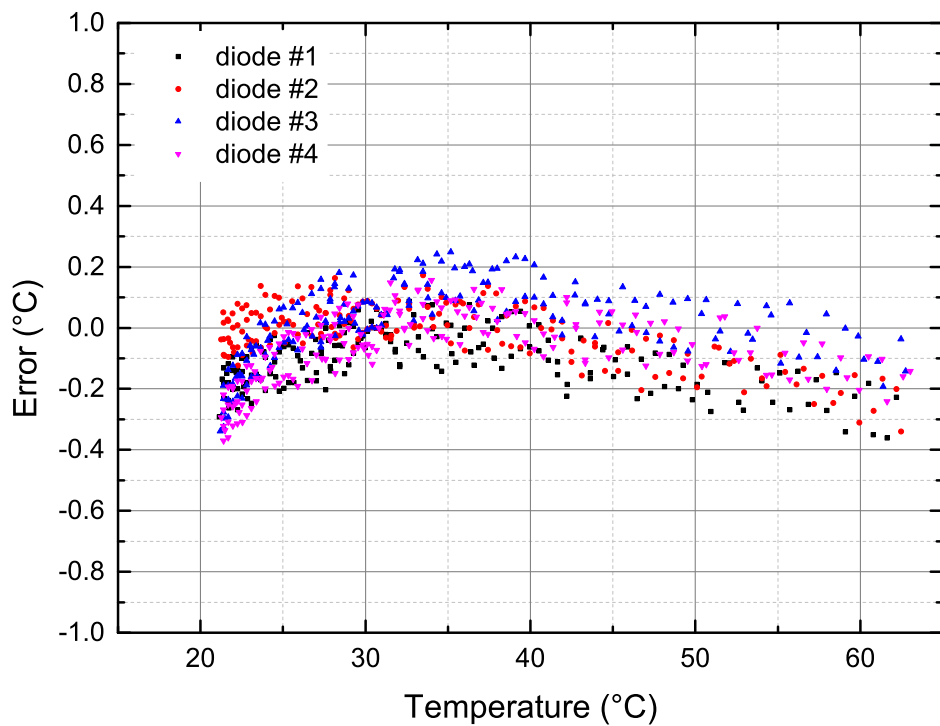


Figure 6.12: Temperature measurement error carried out by calibrated diodes over desired temperature range.

## 7. Calibration procedures

The chapter describes procedures and methods of calibrations utilizing the test and calibration stand. At this point characteristics of the stand are assumed as known and well-defined, thus only a guidelines for a CD4007 characterisation are presented.

### 7.1. Temperature dependence calibrations



Figure 7.1: The CD4007 transistors during temperature calibration.

Calibration techniques for both body diode of N-MOSFET and  $V_{Th}$  temperature dependences are similar. In general, it involves a container with a mineral oil and a heater. The heater heats up the oil to desired, maximal temperature which can be monitored by immersed attachable card board with temperature sensors. Once the desired temperature is achieved, the heater should be turned off and slow self-cooling takes place (assuming a large heat capacity of oil in the container and high thermal resistance). During cooling down the calibration can be carried out - the stand acquires temperature indicated by the reference thermometers and the transistors parameters biased with

a constant current. The acquisition can be done with the stand control panel created in LabVIEW environment. It is assumed that the oil, reference thermometers and CD4007 transistors on the card board at given time are all in thermal equilibrium. The schematic diagram of the procedure is shown in Figure 7.2. If calibration over a range below ambient temperature is needed, the oil can be cooled down to desired minimal temperature instead of heating up.

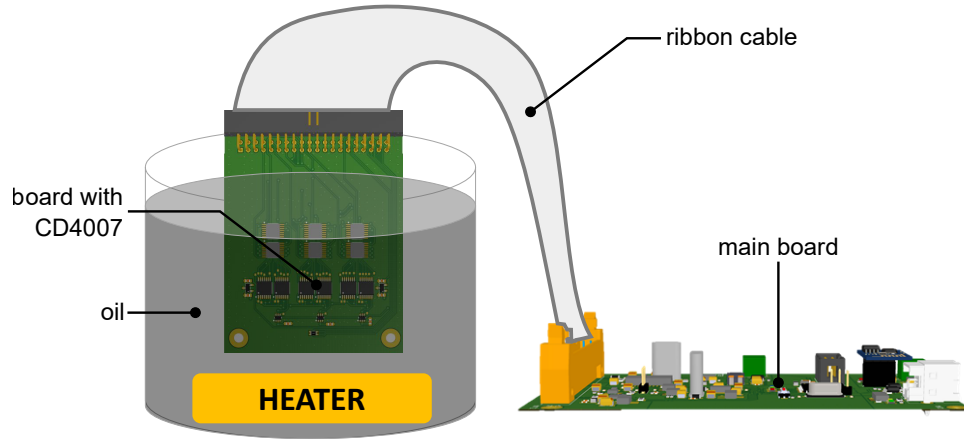


Figure 7.2: The CD4007 transistors during temperature calibration.

## 7.2. Zero-temperature coefficient current determination

The zero-temperature coefficient current ( $I_{ZTC}$ ) determination demands acquisition of transistors  $V_{Th}(T)$  dependence under bias with different currents. Temperature sweep should be performed in exactly the same way as described in chapter 7.1, but it is also necessary to sweep drain current. This functionality is also implemented in the control PC software. Because the sweep in a wide range can take significant amount of time, for a first estimation of  $I_{ZTC}$  number of current values should be limited. Then, based on analyze of rough characteristic, a more narrow range of currents around estimated  $I_{ZTC}$  can be selected and accurately investigated.

## 7.3. Ionising radiation influence calibration

In this type of measurement is important to shield the main board of the stand against radiation. Only the card board should be placed within a main beam. During the calibration a convenient wireless connection may be used. The calibration of  $V_{Th}$  dependence involves an external source of ionising radiation with known dose rate or additional dose rate or TID sensor e.g passive thermoluminescent dosimeter (TLD). For a measurement utilizing TLD, the time of each irradiation session with a constant dose rate should be noted, so the absorbed dose in each session can be determined when the TLD is finally read. Normally in calibration a Co-60 gamma radiation source is utilized.

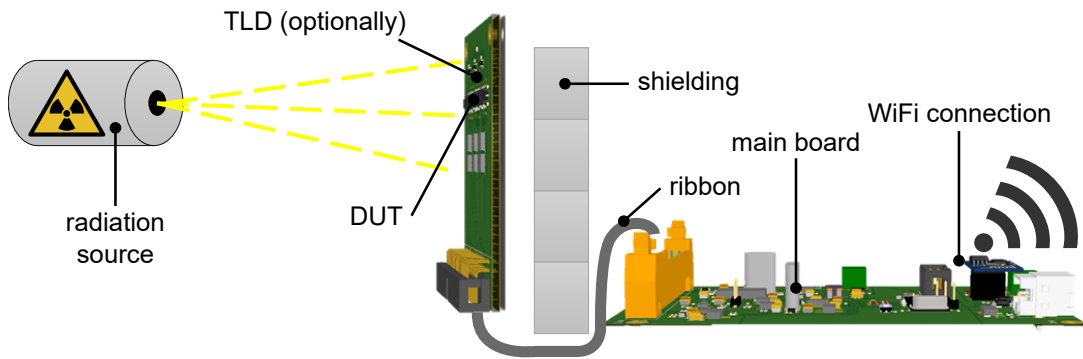


Figure 7.3: The CD4007 transistors during TID calibration.

## **8. Summary**

The thesis describes an early step in a development of low-cost dosimetry system suitable for small satellites deployed on low Earth orbit. The test and calibration stand will allow to test selected transistors, obtain calibration curves and conduct feasibility studies for the whole dosimetry system.

The project has resulted in specified, fully operational and ready to use test and calibration stand. It was designed to work both in a normal conditions of a laboratory room as well as in a harsh, radiation zones during TID calibration. It was possible thanks to careful components selection and organization of whole system. All subsystems were accurately commissioned and their performance was compared with desired values.

First test of the CD4007 integrated circuits conducted utilizing the stand, combined with literature data yields in promising results and conclusions. Further steps in development of dosimetry system for the PW-Sat2 CubeSat assume calibration of numbers of CD4007 integrated circuits by means of thermal and TID calibrations in order to provide accurate and statistically significant data.

Thanks to modular construction and redundant control I/O lines available in IDC socket the stand can be used in calibrations of different transistors and diodes in terms of TID and thermal response.

Development of the system was mainly carried out in Wireless Sensor and Control Networks laboratory at the Department of Electronics, IET Faculty, AGH University of Science and Technology. The first irradiation tests were carried out at the Institute of Nuclear Physics PAN in Krakow. The project was partially supported by Chancellor's grant ("Grant Rektorski").

## Bibliography

- [1] European Space Agency. *Radiation environment*. [http://www.esa.int/Our\\_Activities/Space\\_Engineering\\_Technology/Space\\_Environment/Radiation\\_environment](http://www.esa.int/Our_Activities/Space_Engineering_Technology/Space_Environment/Radiation_environment). [Online; accessed 24-Nov-2016].
- [2] Palma A.J., ed. *Some advances in dose measurement with MOSFET for portable instrumentation*. The First International Conference on Radiation and Dosimetry in Various Fields of Research RAD 2012. 2012, pp. 301–304.
- [3] Boterenbrood H., Hallgren B. *SEE and TID Tests of the Embedded Local Monitor Board with the ATmega128 processor, CERN ATLAS Internal Working Note, DCSIWN20*. <http://atlas.web.cern.ch/Atlas/GROUPS/DAQTRIG/DCS/SEE03-1-report.pdf>. [Online; accessed 20-Nov-2016]. 2003.
- [4] Yadegari B. *Low Power Gamma-Ray FG-MOSFET Dosimeter in 0.13 jum CMOS Technology*. A thesis of M.Sc., Department of Electronics, Carleton University. 2012.
- [5] Siebel O. F., Schneider M. C., Galup-Montoro C., ed. *Low power and low voltage VT extractor circuit and MOSFET radiation dosimeter*. 10th IEEE International NEWCAS Conference. 2012, pp. 301–304.
- [6] Siebel O. F., Schneider M. C., Galup-Montoro C., ed. *Low power and low voltage VT extractor circuit and MOSFET radiation dosimeter*. New Circuits and Systems Conference (NEWCAS), IEEE 10th International. Department of Electrical Engineering, Federal University of Santa Catarina. 2012.
- [7] San Luis Obispo California Polytechnic State University. *CubeSat Design Specification Rev. 13*. 2014.
- [8] FAA William J. Hughes Technical Center. *Single Event Effects Mitigation Techniques Report*. [https://www.faa.gov/aircraft/air\\_cert/design\\_approvals/air\\_software/media/TC-15-62.pdf](https://www.faa.gov/aircraft/air_cert/design_approvals/air_software/media/TC-15-62.pdf). [Online; accessed 25-Nov-2016]. 2016.
- [9] Atmel Corporation. *AVR121: Enhancing ADC resolution by oversampling - Application Note*. <http://www.atmel.com/images/doc8003.pdf>. 2005.
- [10] Badhwar G. D. “The Radiation Environment in Low-Earth Orbit”. *Radiation Research* 148.5s (1997), S3–S10.
- [11] Carvajal M. A., Martinez-Garcia M. S., Guirado D. “Dose verification system based on MOS transistor for real-time measurement”. *Sensors and Actuators: A Physical* (2016).

- [12] Makowski D. *The Impact on Electronic Devices with the Special Consideration of Neutron and Gamma Radiation Monitoring*. A thesis of Ph.D., Department of Microelectronics and Computer Science, Technical University of Lodz. 2006.
- [13] Analog Devices. *Image of a functional diagram of CD4007 integrated circuit*. <https://wiki.analog.com/university/courses/electronics/electronics-lab-28>. [Online; accessed 20-Nov-2016].
- [14] Analog Devices. *In-Amp Input RFI Protection*. <http://www.analog.com/media/en/training-seminars/tutorials/MT-070.pdf>. [Online; accessed 20-Nov-2016]. 2009.
- [15] Murnane M., Analog Devices. *AN-968: Current Sources: Options and Circuits*. <http://www.analog.com/media/en/technical-documentation/application-notes/AN-968.pdf>. 2008.
- [16] Feinendegen L. E. “Evidence for beneficial low level radiation effects and radiation hormesis”. *The British Journal of Radiology* 78.925 (2005), pp. 3–7.
- [17] Espressif. *ESP8266EX Datasheet, Version 5.2*. [http://espressif.com/sites/default/files/documentation/0a-esp8266ex\\_datasheet\\_en.pdf](http://espressif.com/sites/default/files/documentation/0a-esp8266ex_datasheet_en.pdf). [Online; accessed 20-Nov-2016]. 2016.
- [18] Benton E.R, Benton E.V. “Space radiation dosimetry in low-Earth orbit and beyond”. *Nuclear Instruments and Methods in Physics Research Section B: Beam Interactions with Materials and Atoms* 184.1–2 (2001). Advanced Topics in Solid State Dosimetry, pp. 255 –294.
- [19] Agarwal S. G., Irom F., ed. *Compendium of Single-Event Latchup and Total Ionizing Dose Test Results of Commercial Analog to Digital Converters*. IEEE Nuclear and Space Radiation Effects Conference (NSREC 2012). 2012.
- [20] Gajoch G. *Total Ionizing Dose (TID) Sensor for Cubesat Nano-Satellites*. A thesis of B.Sc., Faculty of Computer Science, Electronics and Telecommunications, AGH University of Science and Technology in Krakow. 2017.
- [21] Zumbahlen H. “Staying Well Grounded”. *Analog Dialogue* 46 (2012).
- [22] T. Huen. “Semiconductor Diode Low Temperature Thermometer”. *Review of Scientific Instruments* 41.9 (1970), pp. 1368–1369.
- [23] *Image of ESP8266 module*. <https://evomedia.evothings.com/2015/07/esp8266.jpg>. [Online; accessed 20-Nov-2016].
- [24] Acromag Incorporated. *Criteria for temperature sensor selection of T/C and RTD sensor types*. [https://www.acromag.com/sites/default/files/RTD\\_Temperature\\_Measurement\\_917A.pdf](https://www.acromag.com/sites/default/files/RTD_Temperature_Measurement_917A.pdf). [Online; accessed 20-Nov-2016]. 2011.
- [25] Falin J., Texas Instruments. *Reverse Current/Battery Protection Circuits*. <http://www.ti.com/lit/an/slva139/slva139.pdf>. [Online; accessed 20-Nov-2016]. 2003.
- [26] Texas Instruments. *LM60 and LM60-Q1 2.7-V, SOT-23 or TO-92 Temperature Sensor Datasheet*. <http://www.ti.com/lit/ds/symlink/lm60.pdf>. [Online; accessed 20-Nov-2016]. 2004.

- [27] Maxim Integrated. *Datasheet: MAX31865 Resistance to digital*. <https://datasheets.maximintegrated.com/en/ds/MAX31865.pdf>. [Online; accessed 20-Nov-2016]. 2015.
- [28] Martínez-García M. S., Carvaja M. A., Simancas F., Banqueri J., Lallena A.M., Palma A. J., ed. *Techniques to increase the sensitivity for dosimetry sensors*. International Work-Conference on Bioinformatics and Biomedical Engineering (IWBBIO). Departamento de Electrónica y Tecnología de Computadores, ET-SIIT, Universidad de Granada. 2013.
- [29] Sze S. M. , Ng K. K. *Physics of Semiconductor Devices, Second Eition*. John Wiley & Sons, 1981. Chap. Chapter 8, pp. 431–510.
- [30] Kayali S., NASA Jet Propulsion Laboratory. *Space Radiation Effects on Microelectronics*. [http://parts.jpl.nasa.gov/docs/Radcrs\\_Final.pdf](http://parts.jpl.nasa.gov/docs/Radcrs_Final.pdf). [Online; accessed 22-Nov-2016].
- [31] Future Technology Devices International Ltd. *FT231X (USB to FULL HANDSHAKE UART IC) Datasheet*. [http://www.ftdichip.com/Support/Documents/DataSheets/ICs/DS\\_UMFT231XA.pdf](http://www.ftdichip.com/Support/Documents/DataSheets/ICs/DS_UMFT231XA.pdf). [Online; accessed 20-Nov-2016]. 2013.
- [32] Świetlik M. *A render of PW-Sat2 satellite*. Internal resources of the PW-Sat2 team.
- [33] Martínez-García M.S., Simancas F., Palma A.J., Lallena A.M., Banqueri J., Carvajal M.A. “General purpose MOSFETs for the dosimetry of electron beams used in intra-operative radiotherapy”. *Sensors and Actuators: A Physical* 210 (2014), 175 — 181.
- [34] Fox K. C., NASA. *NASA’s Van Allen Probes Spot an Impenetrable Barrier in Space*. <https://www.nasa.gov/content/goddard/van-allen-probes-spot-impenetrable-barrier-in-space>. [Online; accessed 24-Nov-2016]. 2014.
- [35] Riebeek H., NASA. *Catalog of Earth Satellite Orbits*. <http://earthobservatory.nasa.gov/Features/OrbitsCatalog/>. [Online; accessed 24-Nov-2016]. 2009.
- [36] Stassinopoulos E. G., Raymond J. P. “The space radiation environment for electronics”. *Proceedings of the IEEE* 76.11 (1988), pp. 1423–1442.
- [37] Wolpert D. , Ampadu P. *Managing Temperature Effects in Nanoscale Adaptive Systems*. Springer-Verlag New York, 2012.
- [38] Premier Farnell plc. *Image of PIK0.0805.2P.A RTD Sensor*. <http://uk.farnell.com/ist-innovative-sensor-technology/pik0-0805-2p-a/sensor-pt1000-smd0805-class-a/dp/1266951>. [Online; accessed 20-Nov-2016].
- [39] Maurer R. H., Fraeman M. E., Martin M. N., Roth D. R. “Harsh Environments: Space Radiation Environments, Effects, and Mitigation”. *Johns Hopkins APL Technical Digest* 28.1 (2008), pp. 17 –29.
- [40] Bedingfield K.L., Leach R.D. *Spacecraft System Failures and Anomalies Attributed to the Natural Space Environment*. NASA Reference Publication 1390. 1996.
- [41] Mitev G.M., Sarieva-Jordanova S. “Enhanced Read-Out System for RADFET Dosimeters Research”. *Annual Journal of Electronics* (2015).

- [42] Ortiz-Conde A., García-Sánchez F. J., Muci J., Barrios A. T., Liou J. J., Ho C. S. “Revisiting MOSFET threshold voltage extraction methods”. *Microelectronics Reliability* 53.1 (2013). Reliability of Micro-Interconnects in 3D IC Packages, pp. 90 –104.
- [43] Ristic G. S. “pMOS dosimeters (RADFETs)” (2015). Applied Physics Laboratory, Faculty of Electronic Engineering, University of Nis, Serbia.
- [44] PW-Sat2 Team. *Website of PW-Sat2 project*. <http://pw-sat.pl>. [Online; accessed 29-Nov-2016]. 2017.
- [45] Holbert K. E., Arizona State University. *Single Event Effects, EEE598 Course*. <http://holbert.faculty.asu.edu/eee560/see.html>. [Online; accessed 25-Nov-2016]. 2006.
- [46] Holbert K. E., Arizona State University. *TID, EEE598 Course*. <http://holbert.faculty.asu.edu/eee560/tiondose.html>. [Online; accessed 25-Nov-2016]. 2006.
- [47] Deme S., Apáthy I., Pázmándi T., Benton E. R., Reitz G., Akatov Y. “On-board TLD measurements on MIR and ISS”. *Radiation Protection Dosimetry* 120 (2006), pp. 438–441.